Scientific Reports

https://doi.org/10.1038/s41598-026-46812-3

Article in Press

Dynamic response of tri-layered functionally graded-viscoelastic-piezomagnetic cylindrical tunnel excited by circumferential shear horizontal waves

Received: 1 December 2025

Accepted: 27 March 2026

Published online: 18 April 2026

Cite this article as: Gupta V., Flah A., Yaylacı M. *et al.* Dynamic response of tri-layered functionally graded-viscoelastic-piezomagnetic cylindrical tunnel excited by circumferential shear horizontal waves. *Sci Rep* (2026). https://doi.org/10.1038/s41598-026-46812-3

Vipin Gupta, Aymen Flah, Murat Yaylacı, Abhik Sur, Ivo Pergl, Mohammad Ghatasheh & Soumik Das

We are providing an unedited version of this manuscript to give early access to its findings. Before final publication, the manuscript will undergo further editing. Please note there may be errors present which affect the content, and all legal disclaimers apply.

If this paper is publishing under a Transparent Peer Review model then Peer Review reports will publish with the final article.

ARTICLE IN PRESS

© The Author(s) 2026. **Open Access** This article is licensed under a Creative Commons Attribution-NonCommercial-NoDerivatives 4.0 International License, which permits any non-commercial use, sharing, distribution and reproduction in any medium or format, as long as you give appropriate credit to the original author(s) and the source, provide a link to the Creative Commons licence, and indicate if you modified the licensed material. You do not have permission under this licence to share adapted material derived from this article or parts of it. The images or other third party material in this article are included in the article's Creative Commons licence, unless indicated otherwise in a credit line to the material. If material is not included in the article's Creative Commons licence and your intended use is not permitted by statutory regulation or exceeds the permitted use, you will need to obtain permission directly from the copyright holder. To view a copy of this licence, visit http://creativecommons.org/licenses/by-nc-nd/4.0/.

ARTICLE IN PRESS

Dynamic Response of Tri-layered Functionally Graded-Viscoelastic-Piezomagnetic Cylindrical Tunnel Excited by Circumferential Shear Horizontal Waves

Vipin Gupta[1], Aymen Flah[2,3,4], Murat Yaylacı [5], Abhik Sur[6], Ivo Pergl[7], Mohammad Ghatasheh[8], Soumik Das [9,*]

[1]*Department of Mathematics, Gurugram University, Gurugram, India*
[2]*Applied Science Research Center, Applied Science Private University, Amman, 11931, Jordan*
[3]*National Engineering School of Gabès, University of Gabès, Tunisia*
[4]*Centre for Research Impact and Outcome, Chitkara University, Punjab University, Punjab, Rajpura, 140401, India*
[5]*Department of Civil Engineering, Recep Tayyip Erdogan University, 53100, Rize, Turkey*
[6] *Department of Mathematics, Sister Nivedita University, West Bengal, India*
[7]*ENET Centre, CEET, VSB-Technical University of Ostrava, 708 00 Ostrava, Czech Republic*
[8]*Department of Basic Sciences, Middle East University, Amman 11831, Jordan*
[9]*School of Physical Sciences, Amrita Vishwa Vidyapeetham, Mysuru campus, Karnataka, India*

[*]***Corresponding author,*** *Email: soumikdas@my.amrita.edu , soumikdas1993@gmail.com*

Abstract: This manuscript presents a detailed analytical study on the propagation behavior of circumferential shear horizontal (SH) waves in a tri-layered cylindrical composite structure, comprising an inner functionally graded (FG) layer, a viscoelastic (VE) middle layer, and an initially stressed piezomagnetic (PM) outer layer. Unlike prior studies that primarily focus on phase velocity analysis, this work offers a novel and in-depth exploration of stress distribution characteristics across the multilayered system. The model incorporates both mechanical and magneto-mechanical interface imperfections and examines the effects of geometric dimensions, material gradation, angular wave modes, and initial stresses on wave dynamics. A robust mathematical framework is developed using the equations of motion and constitutive relations specific to each material, leading to a dispersion relation formulated under suitable boundary conditions. Numerical simulations demonstrate that the phase velocity and surface wave responses are notably influenced by gradation parameters, layer radii, and imperfection factors. Most significantly, detailed stress profiles are constructed to reveal how material damping, gradation, and interface conditions interact to shape the internal stress landscape. This dual-phase velocity and stress analysis offers enhanced insight into wave–material interactions, providing a valuable design reference for next-generation piezomagnetic sensors, actuators, and composite structural components.

Keywords: SH-waves; Interface imperfections; Viscoelastic material; Functionally graded material; Piezomagnetic material; Composite cylinder.

ARTICLE IN PRESS

1. Introduction

SH wave propagation has emerged as a critical research area due to its applicability in structural health monitoring, seismic analysis, and advanced device design [1], [2], [3]. Unlike longitudinal or Rayleigh waves, SH-waves propagate with particle motion perpendicular to the direction of propagation and are less influenced by surface conditions, making them ideal for characterizing subsurface or interfacial features [4], [5]. Several studies have extensively analyzed the dispersive and damping behaviors of SH-waves [6], [7], [8]. In parallel, researchers have investigated a broad range of structural dynamics issues, such as vortex-induced vibrations in risers [9], vibration characteristics of damped systems [10], and discrete wave dynamics in mechanical chains [11]. Despite the technical sophistication of these models, most assume perfectly bonded interfaces. However, in realistic engineering and geological settings, interfaces often exhibit imperfections, such as voids, cracks, or partial bonding that can significantly alter wave propagation characteristics [12], [13]. These interfacial discontinuities play a decisive role in modulating both the phase velocity and the stress distribution of SH-waves, thereby necessitating a deeper investigation into their coupled effects. Recent developments in smart sensing materials and structural health monitoring systems have highlighted the importance of coupled stress–wave behavior and multifunctional structural responses in engineering applications [14], [15], [16], [17].

SH waves have been extensively investigated in cylindrical structures due to their unique polarization perpendicular to the propagation direction and circumferential symmetry, which make them highly suitable for applications in sensing, non-destructive evaluation, and wave guiding devices [18]. In recent years, smart material composite materials have attracted significant attention for their superior mechanical performance, tunable wave propagation characteristics, and multifunctional capabilities. Tong *et al.* [19] expanded this framework to include multiphase cylindrical models examining thermal, magnetic, and mechanical interactions in fiber composites. In underground infrastructure and geomechanical engineering, data-driven prediction techniques and advanced diagnostic methods have been widely employed to analyze tunnel stability, pipeline settlement, and rock damage evolution under dynamic loading conditions [20], [21], [22]. Furthermore, modern studies on wave propagation, structural optimization, vibration characteristics, and electro-mechanical interactions in composite and piezoelectric media demonstrate the growing relevance of multiphysics wave analysis in complex structural configurations [23], [24], [25] [26], [27].

Recent studies have extensively investigated the dynamic behavior and mechanical response of advanced shell and curved structures under various loading conditions. Analytical

ARTICLE IN PRESS

and computational models for cylindrical, conical, and spherical shells have demonstrated significant applications in vibration analysis, structural stability, and multifunctional composite systems [28], [29], [30], [31], [32]. These contributions highlight the growing importance of shell-based configurations in modern engineering and motivate further investigation of wave propagation phenomena in multilayer cylindrical structures. The study of wave dynamics in cylindrical geometries is critical across diverse domains, including structural engineering, materials science, geophysics, biomedical engineering, nanotechnology, acoustics, and applied physics [33], [34], [35]. Viscoelastic materials have emerged as an essential component in controlling dynamic behavior in composite cylindrical structures due to their inherent damping capabilities and time-dependent mechanical response [36], [37]. Akbarov and Kepceler [38] analyzed torsional wave characteristics in hollow viscoelastic cylinders, while Zhang *et al.* [39] studied guided wave behavior in Kelvin-Voigt (KV) viscoelastic cylinders featuring material gradation.

Material gradation has been widely investigated as a means to tailor mechanical and electro-mechanical, and magneto-mechanical behavior in cylindrical structures. Notably, Khoshgoftar *et al.* [40] analyzed the impact of graded material properties on thermoelastic responses in piezoelectric cylinders, while Othman and Abbas [41] discussed how non-uniform material characteristics influence the response of isotropic cylinders subjected to thermal shock using finite element methods. Guo *et al.* [42] probed into the influence exerted by functionally graded intermediate layers on the governing SH waves within layered piezoelectric/piezomagnetic cylinders. Mahanty *et al.* [43] probed into shear acoustic wave conveyance through layered cylindrical configurations exhibiting imperfect bonding between functionally graded piezoelectric material (FGPM) strata. Gupta and his team study various problem related to wave dynamics in piezo-thermoelastic media [44], [45], [46], [47], [48]. Recently, Kumawat and Vishwakarma [49], Gupta *et al.* [50] scrutinized SH-wave propagation across multi-layered cylinders.

Moreover, although several previous studies have analyzed SH-wave dispersion, their focus has predominantly been limited to calculating the phase velocity. The specific influence of the gradation parameter on wave dynamics and surface responses remains insufficiently explored, particularly in configurations incorporating viscoelastic damping and interfacial imperfections. Motivated by these gaps, the present study investigates SH-wave propagation in a tri-layered cylindrical composite comprising an inner functionally graded layer, a viscoelastic middle layer, and an initially stressed piezomagnetic outer layer. A mathematical

ARTICLE IN PRESS

model is developed to derive dispersion relations while rigorously incorporating mechanical and magneto-mechanical interface imperfections.

2. Modeling of the Structural Geometry

The physical setup is a tri-layered cylindrical construct featuring concentric arrangements: an internal functionally graded (FG) layer, an orthotropic viscoelastic (VE) material middle layer, and an externally positioned, initially stressed piezomagnetic (PM) layer. The FG layer has a thickness of $(r_1 - r_0)$, enclosed by the VE layer having a thickness of $(r_2 - r_1)$. The outermost PM layer has a thickness of $(r_3 - r_2)$, as shown in Fig. 1. Due to the significantly smaller cross-sectional dimensions compared to their axial lengths, the cylinders are idealized as infinitely extended along the longitudinal direction. The concentric layers are assumed to be imperfectly bonded at their interfaces, giving rise to discontinuities in both mechanical and magneto-mechanical interactions. The entire system is analyzed within a cylindrical coordinate framework (r, θ, z), where the origin O is positioned along the central axis of the structure. In this study, the SH-wave is considered to propagate along the circumferential (θ) direction with particle motion in the axial (z) direction, perpendicular to the plane of propagation, satisfying the condition of shear horizontal motion in a cylindrical structure. As a result, wave displacement is confined to the $z-$direction. Thus, the displacement components given as [51]

$$u_r^{(m)} = 0\,,\; u_\theta^{(m)} = 0\,,\; u_z^{(m)} = u_z^{(m)}(r,\theta,t)\,, \tag{2.1}$$

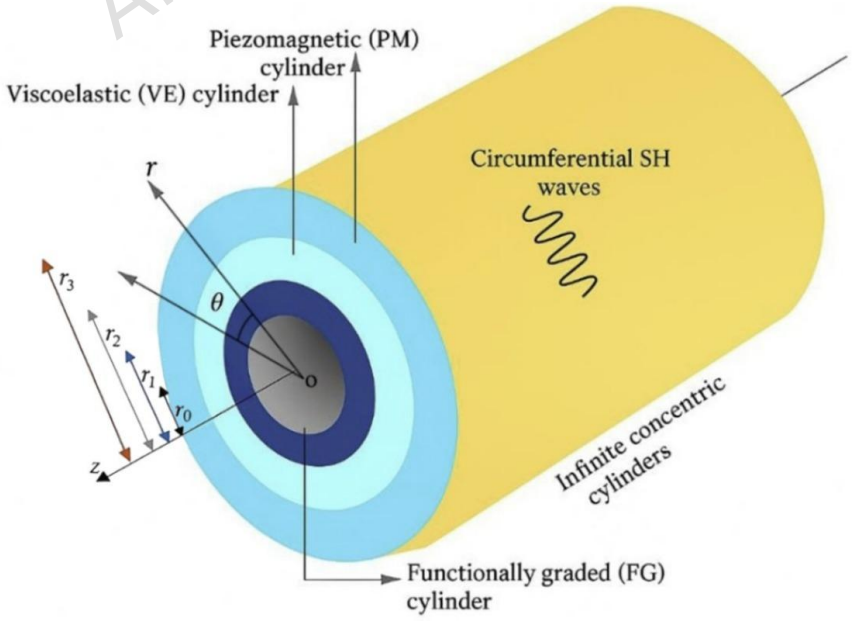


Fig. 1: Geometry of the problem

ARTICLE IN PRESS

where $u_r^{(m)}$, $u_\theta^{(m)}$, and $u_z^{(m)}$ indicate the components of mechanical displacement along the radial r, circumferential θ, and axial z directions, respectively, within the designated material layer m. In this context, $m=1,2,3$ signify the FG material, the VE material, and the initially stressed PM material, respectively. By adopting this simplification, the study emphasizes the axial displacement component $u_z^{(m)}$, considered as a function of radial r, circumferential θ, and longitudinal coordinates z.

2.1 Displacement Characteristics of the FG Medium

To establish the displacement field associated with SH waves within the FG orthotropic cylindrical segment, the equation of motion [52], denoted here with superscript $m=1$,

$$\sigma_{rz}^{(1)},_r+\frac{\sigma_{rz}^{(1)}}{r}+\frac{\sigma_{\theta z}^{(1)},_\theta}{r}=\rho^{(1)}\ddot{u}_z\,, \tag{2.1.1}$$

where σ_{rz}, $\sigma_{\theta z}$ signifies the component of stress tensor, subscripts after commas represent derivatives taken in the direction of the specified coordinate, and overdots denote time derivatives.

The stress–displacement relation, as outlined by Li and Wang [53], is obtained through equation (2.1)

$$\sigma_{rz}^{(1)}=c_{44}^{(1)}u_z^{(1)},_r\,,\quad \sigma_{\theta z}^{(1)}=\frac{c_{55}^{(1)}}{r}u_z^{(1)},_\theta\,. \tag{2.1.2}$$

The functionally graded nature of the layer $(r_0<r<r_1)$ is intended to enhance the attributes of the FG medium. Consequently, all material properties along the $r-$ direction are taken as

$$c_{44}^{(1)}=c_{44}^{(F)}\left(\frac{r}{r_1}\right)^{l_1},\ c_{55}^{(1)}=c_{55}^{(F)}\left(\frac{r}{r_1}\right)^{l_1},\ \rho^{(1)}=\rho^{(F)}\left(\frac{r}{r_1}\right)^{l_1}, \tag{2.1.3}$$

where $c_{44}^{(1)}$, $c_{55}^{(1)}$ represent the elastic shear modulus and $\rho^{(1)}$ is the density, of the FG layer. The terms $c_{44}^{(F)}$, $c_{55}^{(F)}$, and $\rho^{(F)}$ denote respective values evaluated at $r=r_1$. Here, l_1 denotes a non-dimensional parameter characterizing the functional gradation.

Equations (2.1.2) and (2.1.3), when substituted into (2.1.1), gives

$$c_{44}^{(F)}\left[r^2u_z^{(1)},_{rr}+r(1+l_1)u_z^{(1)},_r\right]+c_{55}^{(F)}u_z^{(1)},_{\theta\theta}=r^2\rho^{(F)}\ddot{u}_z^{(1)}. \tag{2.1.4}$$

In order to proceed, the following functional form of the solution is assumed

ARTICLE IN PRESS

$$u_z^{(1)}\left(r,\theta,t\right)=W^{(1)}\left(r\right)\exp\left[\iota\left(n\theta-\omega t\right)\right]r^{-l_1/2}. \tag{2.1.5}$$

In this expression, $W^{(1)}$ denote the arbitrary function, n is a non-negative real value, ω indicates angular frequency, and t stands for time.

Incorporating equation (2.1.5) into (2.1.4) and simplifying gives

$$r^2W^{(1)},_{rr}+rW^{(1)},_r+\left[\frac{r^2\omega^2}{\beta_1^2}-\left(c^2n^2+\frac{l^2}{4}\right)\right]W^{(1)}=0, \tag{2.1.6}$$

where $\beta_1^2=\frac{c_{44}^{(F)}}{\rho^{(1)}}$, $c^2=\frac{c_{55}^{(F)}}{c_{44}^{(F)}}$.

This equation can be seen to be an instance of Bessel's differential equation of order $p_1\left(=\sqrt{\left(c^2n^2+\frac{l_1^2}{4}\right)}\right)$, and its solution takes the form

$$W^{(1)}\left(r\right)=C_1^{(1)}J_{p_1}\left(\frac{r\omega}{\beta_1}\right)+C_2^{(2)}Y_{p_1}\left(\frac{r\omega}{\beta_1}\right), \tag{2.1.7}$$

where $C_1^{(1)}$ and $C_2^{(1)}$ are unknown constants, while $J_{p_1}(.)$ and $Y_{p_1}(.)$ denote Bessel functions of the first and second kind, respectively, both of order p_1.

Hence, the FG material layer's $\left(r_0<r<r_1\right)$ displacement component is formulated as

$$u_z^{(1)}=\left[C_1^{(1)}J_{p_1}\left(\frac{r\omega}{\beta_1}\right)+C_2^{(1)}Y_{p_1}\left(\frac{r\omega}{\beta_1}\right)\right]r^{-l_1/2}\exp\left[\iota\left(n\theta-\omega t\right)\right]. \tag{2.1.8}$$

ARTICLE IN PRESS

2.2 Displacement Characteristics of the Viscoelastic (VE) Medium

The SH-wave displacement in the orthotropic viscoelastic cylinder is obtained using the equation of motion [52], with the superscript $m=2$

$$\sigma_{rz}^{(2)},_r+\frac{\sigma_{rz}^{(2)}}{r}+\frac{\sigma_{\theta z}^{(2)},_\theta}{r}=\rho^{(2)}\ddot{u}_z^{(2)}. \tag{2.2.1}$$

According to the Kelvin–Voigt viscoelastic model [39], the constitutive equation is given by

$$\sigma_{ij}^{(2)}=\bar{c}_{ijkl}\varepsilon_{kl}^{(2)}, \tag{2.2.2}$$

where $\bar{c}_{ijkl}=c_{ijkl}^{(2)}+\mu_{ijkl}^{(2)}\frac{\partial}{\partial t}$. Here, $\mu_{ijkl}^{(2)}$ is the viscosity parameter and $\varepsilon_{kl}^{(2)}$ is the strain tensor.

In light of equations (2.1) and (2.2.2), the stress–displacement relationship can be expressed as

ARTICLE IN PRESS

$$\sigma_{rz}^{(2)} = \bar{c}_{44}^{(2)} u_z^{(2)},_r, \quad \sigma_{\theta z}^{(2)} = \frac{\bar{c}_{55}^{(2)}}{r} u_z^{(2)},_\theta . \tag{2.2.3}$$

Thus, utilizing equations (2.1) and (2.2.3) into the equation (2.2.1), we get

$$r^2 u_z^{(2)},_{rr} + \frac{\bar{c}_{55}^{(2)}}{\bar{c}_{44}^{(2)}} u_z^{(2)},_{\theta\theta} + r u_z^{(2)},_r = \frac{r^2 \rho^{(2)}}{\bar{c}_{44}^{(2)}} \ddot{u}_z^{(2)} . \tag{2.2.4}$$

Now, let us assume a solution of the form

$$u_z^{(2)}(r,\theta,t) = W^{(2)}(r) \exp\left[\iota(n\theta - \omega t)\right], \tag{2.2.5}$$

where $W^{(2)}$ denote the arbitrary function.

Inserting the solution (2.2.5) into equation (2.2.4) and simplifying yields

$$r^2 W^{(2)},_{rr} + r W^{(2)},_r + \left[\frac{r^2\omega^2}{\beta_2^2} - c_1^2 n^2\right] W^{(2)} = 0, \tag{2.2.6}$$

where $\beta_2^2 = \dfrac{\bar{c}_{44}^{(2)}}{\rho^{(2)}}$, $c_1^2 = \dfrac{\bar{c}_{55}^{(2)}}{\bar{c}_{44}^{(2)}}$, $\bar{c}_{44}^{(2)} = c_{44}^{(2)} - i\omega\mu_{44}^{(2)}$, $\bar{c}_{55}^{(2)} = c_{55}^{(2)} - i\omega\mu_{55}^{(2)}$.

This equation represents a differential equation of Bessel form with order $p_2 (= c_1 n)$, and its solution takes the form

$$W^{(2)} = C_1^{(2)} J_{p_2}\left(\frac{r\omega}{\beta_2}\right) + C_2^{(2)} Y_{p_2}\left(\frac{r\omega}{\beta_2}\right), \tag{2.2.7}$$

where $C_1^{(2)}$ and $C_2^{(2)}$ are unknown constants, while $J_{p_2}(.)$ and $Y_{p_2}(.)$ denote Bessel functions of the first and second kind, respectively, both of order p_2.

Hence, the VE material layer's $(r_1 < r < r_2)$ displacement component is formulated as

$$u_z^{(2)} = \left[C_1^{(2)} J_{p_2}\left(\frac{r\omega}{\beta_2}\right) + C_2^{(2)} Y_{p_2}\left(\frac{r\omega}{\beta_2}\right)\right] \exp\left[\iota(n\theta - \omega t)\right]. \tag{2.2.8}$$

2.3 Displacement Characteristics of the Initially Stressed Piezomagnetic (PM) Medium

The equations governing motion in the initially stressed piezomagnetic medium, excluding body forces, and Gauss's law under charge-free conditions, can be written as [54]

$$\sigma_{ij}^{(3)},_j + \left(u_i^{(3)},_k \sigma_{kj}^{(0)}\right),_j = \rho^{(3)} \ddot{u}_i^{(3)}, \tag{2.3.1}$$

$$\sigma_{ij}^{(3)},_j + \left(u_i^{(3)},_{kj} \sigma_{kj}^{(0)}\right) + \left(u_i^{(3)},_k \sigma_{kj,j}^{(0)}\right) = \rho^{(3)} \ddot{u}_i^{(3)}, \tag{2.3.2}$$

ARTICLE IN PRESS

$$\frac{\partial}{\partial r}\left[\sigma_r^{(0)}u_r^{(3)},_r+\sigma_{r\theta}^{(0)}\frac{u_r^{(3)},_\theta-u_\theta^{(3)}}{r}+\sigma_{rz}^{(0)}u_r^{(3)},_z+\sigma_r^{(3)}\right]+\frac{\partial}{r\partial\theta}\left[\sigma_{r\theta}^{(0)}u_r^{(3)},_r+\sigma_\theta^{(0)}\frac{u_r^{(3)},_\theta-u_\theta^{(3)}}{r}+\sigma_{\theta z}^{(0)}u_r^{(3)},_z+\sigma_{r\theta}^{(3)}\right]$$
$$+\frac{\partial}{\partial z}\left[\sigma_{zr}^{(0)}u_r^{(3)},_r+\sigma_{\theta z}^{(0)}\frac{u_r^{(3)},_\theta-u_\theta^{3}}{r}+\sigma_z^{(0)}u_r^{(3)},_z+\sigma_{zr}^{(3)}\right]+$$
$$\frac{1}{r}\left[\sigma_r^{(0)}u_r^{(3)},_r+\sigma_{r\theta}^{(0)}\frac{u_r^{(3)},_\theta-u_\theta^{(3)}}{r}+\sigma_{zr}^{(0)}u_r^{(3)},_z-\sigma_{r\theta}^{(0)}u_\theta^{(3)},_r-\sigma_\theta^{(0)}\frac{u_r^{(3)}+u_\theta^{(3)},_\theta}{r}-\sigma_{\theta z}^{(0)}u_\theta^{(3)},_z+\sigma_r^{(3)}-\sigma_\theta^{(3)}\right]=\rho^{(3)}\ddot{u}_r^{(3)} \tag{2.3.3}$$

$$\frac{\partial}{\partial r}\left[\sigma_r^{(0)}u_\theta^{(3)},_r+\sigma_{r\theta}^{(0)}\frac{u_r^{(3)}+u_\theta^{(3)},_\theta}{r}+\sigma_{rz}^{(0)}u_\theta^{(3)},_z+\sigma_{r\theta}^{(3)}\right]+\frac{\partial}{r\partial\theta}\left[\sigma_{r\theta}^{(0)}u_\theta^{(3)},_r+\sigma_\theta^{(0)}\frac{u_r^{(3)}+u_\theta^{(3)},_\theta}{r}+\sigma_{\theta z}^{(0)}u_\theta^{(3)},_z+\sigma_{\theta\theta}^{(3)}\right]$$
$$+\frac{\partial}{\partial z}\left[\sigma_{zr}^{(0)}u_\theta^{(3)},_r+\sigma_{\theta z}^{(0)}\frac{u_r^{(3)}+u_{\theta,\theta}}{r}+\sigma_z^{(0)}u_\theta^{(3)},_z+\sigma_{zz}^{(3)}\right]+$$
$$\frac{1}{r}\left[\sigma_r^{(0)}u_\theta^{(3)},_r+\sigma_{r\theta}^{(0)}\frac{u_r^{(3)}+u_\theta^{(3)},_\theta}{r}+\sigma_{zr}^{(0)}u_\theta^{(3)},_z+\sigma_{r\theta}^{(0)}u_r^{(3)},_r+\sigma_{\theta\theta}^{(0)}\frac{u_r^{(3)},_\theta-u_\theta^{(3)}}{r}+\sigma_{\theta z}^{(0)}u_r^{(3)},_z+2\sigma_{r\theta}^{(3)}\right]=\rho^{(3)}\ddot{u}_\theta^{(3)} \tag{2.3.4}$$

$$\frac{\partial}{\partial r}\left[\sigma_r^{(0)}u_z^{(3)},_r+\sigma_{r\theta}^{(0)}\frac{u_z^{(3)},_\theta}{r}+\sigma_{rz}^{(0)}u_z^{(3)},_z+\sigma_{zr}^{(3)}\right]+\frac{\partial}{r\partial\theta}\left[\sigma_{r\theta}^{(0)}u_z^{(3)},_r+\sigma_\theta^{(0)}\frac{u_z^{(3)},_\theta}{r}+\sigma_{\theta z}^{(0)}u_z^{(3)},_z+\sigma_{\theta z}^{(3)}\right]$$
$$+\frac{\partial}{\partial z}\left[\sigma_{zr}^{(0)}u_z^{(3)},_r+\sigma_{\theta z}^{(0)}\frac{u_z^{(3)},_\theta}{r}+\sigma_z^{(0)}u_z^{(3)},_z+\sigma_{zz}^{(3)}\right]+\frac{1}{r}\left[\sigma_r^{(0)}u_z^{(3)},_r+\sigma_{r\theta}^{(0)}\frac{u_z^{(3)},_\theta}{r}+\sigma_{zr}^{(0)}u_z^{(3)},_z+\sigma_{zr}^{(3)}\right]=\rho^{(3)}\ddot{u}_z^{(3)} \tag{2.3.5}$$

Given that SH-waves travel along the $\theta-$axis, we retain only the invariant axial initial stress $\sigma_\theta^{(0)}$. Thus, by applying equation (2.1), the motion equations simplify to [49]

$$\frac{\partial\sigma_{zr}^{(3)}}{\partial r}+\frac{\sigma_\theta^{(0)}}{r^2}\frac{\partial^2u_z^{(3)}}{\partial\theta^2}+\frac{1}{r}\frac{\partial\sigma_{\theta z}^{(3)}}{\partial\theta}+\frac{\sigma_{zr}^{(3)}}{r}=\rho^{(3)}\left(\frac{\partial^2u_z^{(3)}}{\partial t^2}\right), \tag{2.3.6}$$

$$B_r^{(3)},_r+\frac{1}{r}B_r^{(3)}+\frac{1}{r}\frac{\partial B_\theta^{(3)}}{\partial\theta}=0, \tag{2.3.7}$$

where, B indicate the magnetic displacement.

The constitutive relations are expressed as [49]

$$\sigma_{rz}^{(3)}=c_{44}^{(3)}u_z^{(3)},_r+h_{15}\psi,_r,\ \sigma_{\theta z}^{(3)}=\frac{1}{r}\left(c_{44}^{(3)}u_z^{(3)},_\theta+h_{15}\psi,_\theta\right), \tag{2.3.8}$$

$$B_r^{(3)}=h_{15}u_z^{(3)},_r-\mu_3\psi,_r,\ B_\theta^{(3)}=\frac{1}{r}\left(h_{15}u_z^{(3)},_\theta-\mu_3\psi,_\theta\right), \tag{2.3.9}$$

where μ_3, h_{15} are the magnetic permeability and piezomagnetic coefficient, respectively. ψ signifies the magnetic potential, pertaining of the PM layer.

ARTICLE IN PRESS

ARTICLE IN PRESS

The governing equations for the PM layer are obtained by substituting equations (2.3.8) and (2.3.9) into equations (2.3.6) and (2.3.7), resulting in

$$c_{44}^{(3)}\nabla^2 u_z^{(3)} + h_{15}\nabla^2\psi + \frac{\sigma_\theta^{(0)}}{r^2}u_z^{(3)},_{\theta\theta} = \rho^{(3)}\ddot{u}_z^{(3)}, \tag{2.3.10}$$

$$h_{15}\nabla^2 u_z^{(3)} - \mu_3\nabla^2\psi = 0, \tag{2.3.11}$$

where $\nabla^2 = \frac{\partial^2}{\partial r^2} + \frac{1}{r}\frac{\partial}{\partial r} + \frac{1}{r^2}\frac{\partial^2}{\partial\theta^2}$.

In order to proceed, the following functional form of the solution is assumed

$$\left[\psi, u_z^{(3)}\right](r,\theta,t) = \left[\Psi, W^{(3)}\right](r)\exp\left[\iota\left(n\theta - \omega t\right)\right], \tag{2.3.12}$$

where Ψ and $W^{(3)}$ are the arbitrary functions.

Equation (2.3.10) yields the resulting expression when the assumed solution (2.3.12) is substituted

$$r^2 W^{(3)},_{rr} + rW^{(3)},_r + \left(\xi^2 r^2 - p_3^2\right)W^{(3)} = 0, \tag{2.3.13}$$

where $\xi^2 = \frac{\rho^{(3)}\mu_3\omega^2}{c_{44}^{(3)}\mu_3 + h_{15}^2}$, $p_3^2 = n^2\left(1 + \frac{\mu_3\sigma_\theta^{(0)}}{c_{44}^{(3)}\mu_3 + h_{15}^2}\right)$.

Incorporating equation (2.3.12) into (2.3.11), the resulting expression becomes

$$\left(W^{(3)},_{rr} + \frac{1}{r}W^{(3)},_r - \frac{n^2 W^{(3)}}{r^2}\right) - \frac{\mu_3}{h_{15}}\left(\Psi,_{rr} + \frac{1}{r}\Psi,_r - \frac{n^2\Psi}{r^2}\right) = 0. \tag{2.3.14}$$

Equation (2.3.13) admits the following solution

$$W^{(3)}(r) = C_1^{(3)}J_{p_3}(r\xi) + C_2^{(3)}Y_{p_3}(r\xi), \tag{2.3.15}$$

where $C_1^{(3)}$ and $C_2^{(3)}$ are unknown constants, while $J_{p_3}(.)$ and $Y_{p_3}(.)$ denote Bessel functions of the first and second kind, respectively, both of order p_3.

Hence, the PM material layer's $(r_2 < r < r_3)$ displacement component is formulated as

$$u_z^{(3)} = \left[C_1^{(3)}J_{p_3}(r\xi) + C_2^{(3)}Y_{p_3}(r\xi)\right]\exp\left[\iota\left(n\theta - \omega t\right)\right], \tag{2.3.16}$$

$$\psi = \left[C_1^* r^{-n} + C_2^* r^n + \frac{h_{15}}{\mu_3}\left\{C_1^{(3)}J_{p_3}(r\xi) + C_2^{(3)}Y_{p_3}(r\xi)\right\}\right]\exp\left[\iota\left(n\theta - \omega t\right)\right], \tag{2.3.17}$$

where $C_1^* r^{-n} + C_2^* r^n$ corresponds to the general solution of the equation $r^2\Psi,_{rr} + r\Psi,_r - n^2\Psi = 0$.

3. Boundary Conditions

ARTICLE IN PRESS

ARTICLE IN PRESS

- On the stress-free inner and outer surfaces, the subsequent condition for $r = r_0$ and $r = r_3$

$$\sigma_{rz}^{(1)}(r_0,\theta,t) = 0\,, \tag{3.1}$$

$$\sigma_{rz}^{(3)}(r_3,\theta,t) = 0\,. \tag{3.2}$$

- At $r = r_1$, the contiguous boundary linking the FG and VE cylinders, continuity of stress dictates that

$$\sigma_{rz}^{(1)}(r_1,\theta,t) = \sigma_{rz}^{(2)}(r_1,\theta,t)\,, \tag{3.3}$$

$$\sigma_{rz}^{(2)}(r_1,\theta,t) = \left[w^{(2)} - w^{(1)} \right] \gamma^{(1,2)}(r_1,\theta,t)\,. \tag{3.4}$$

- The magnetic potential vanishes at $r = r_2$. i.e.

$$\psi(r_2,\theta,t) = 0\,, \tag{3.5}$$

whereas at $r = r_2$, the interface between the VE and PM cylinders, the continuity conditions entail

$$\sigma_{rz}^{(3)}(r_2,\theta,t) = \sigma_{rz}^{(2)}(r_2,\theta,t)\,, \tag{3.6}$$

$$\sigma_{rz}^{(3)}(r_2,\theta,t) = \gamma^{(2,3)}(r_2,\theta,t)\left[w^{(3)} - w^{(2)}\right]. \tag{3.7}$$

- The magnetic potential vanishes at $r = r_3$, i.e.

$$\psi(r_3,\theta,t) = 0\,, \tag{3.8}$$

where $\gamma^{(1,2)}$ and $\gamma^{(2,3)}$ designate parameters describing mechanical interface imperfection.

ARTICLE IN PRESS

4.1 Wave Dispersion Analysis

The displacements, stresses, and magnetic potential solution obtained in Section 2 are now implemented within the framework of boundary condition. This process involves the introduction of two dimensionless parameters quantifying interface imperfections, along with a third dimensionless parameter characterizing the initial stress state.

$$\Lambda_1 = \frac{c_{55}^{(F)}}{r_1\gamma^{(1,2)}}\,,\ \Lambda_2 = \frac{c_{44}^{(3)}}{r_2\gamma^{(2,3)}}\,,\ \sigma^* = \frac{\sigma^{(0)}}{c_{44}^{(3)}}\,. \tag{4.1.1}$$

The subsequent formulation of the dispersion relation leads to a system of eight simultaneous equations, each corresponding to a specific boundary condition. The requirement for a non-trivial solution, involving the eight arbitrary constants, necessitates that the determinant of the associated 8 × 8 coefficient matrix equal zero. This constraint gives rise to the following dispersion relation

ARTICLE IN PRESS

$$\det\left(\Upsilon_{uv}\right)=0,\ u,v=1-8. \tag{4.1.2}$$

Detailed expressions for the elements Υ_{uv} are available in the appendix.

4.2 Surface Response

Prior investigations frequently prioritize the dispersion relation while omitting analysis of the surface response, a simplification driven by the intricate nature of multilayered systems. To explore the surface response under the action of external forces, we impose an external mechanical stress $\sigma_{ext}\exp i\left(n\theta-\omega t\right)$ at the inner boundary. This addition enhances analytical depth, while the integrity of the remaining boundary conditions (3.1 through 3.8) is preserved to ensure consistency with the physical model. The derived equations constitute a non-homogeneous system

$$\Upsilon X=Q, \tag{4.2.1}$$

where the explicit forms of Υ, X, and Q can be found in the Appendix. The unknown coefficients are computed using MATLAB through an efficient matrix inversion algorithm, enabling the solution of the non-homogeneous system. Once these coefficients are determined, they are utilized to derive the corresponding stress distribution, offering a comprehensive depiction of the surface response to the applied external mechanical loading.

5. Numerical Simulations and Analyses

To understand the complex behavior of SH-wave propagation in a tri-layered cylindrical structure, this section undertakes a comprehensive computational study focused on key elastic and material parameters. A schematic overview of the system's geometry, including precise dimensions and material distributions for each layer, is provided in Fig. 2. These values are based on established literature, ensuring consistency with prior theoretical and experimental studies [49], [52], [55], [56]. Wave motion within each cylindrical layer is characterized by analytically solving the governing equations under the appropriate boundary conditions, as established in Section 4.1. This process leads to the formulation of a dispersion relation that captures the essential wave mechanics. A comparative evaluation is carried out through dispersion plots, where normalized phase velocity is charted against normalized wavenumber to reveal mode-specific propagation characteristics.

In addition to bulk wave behavior, the study also focuses on the surface response characteristics of the composite system when influenced by SH-wave excitation. Section 4.2 outlines the methodology for generating stress distribution profiles along the surface, enabling insights into how material and structural variations influence wave-induced surface

ARTICLE IN PRESS

dynamics. To ensure practical relevance and a broad applicability of findings, the following parameters were systematically varied:

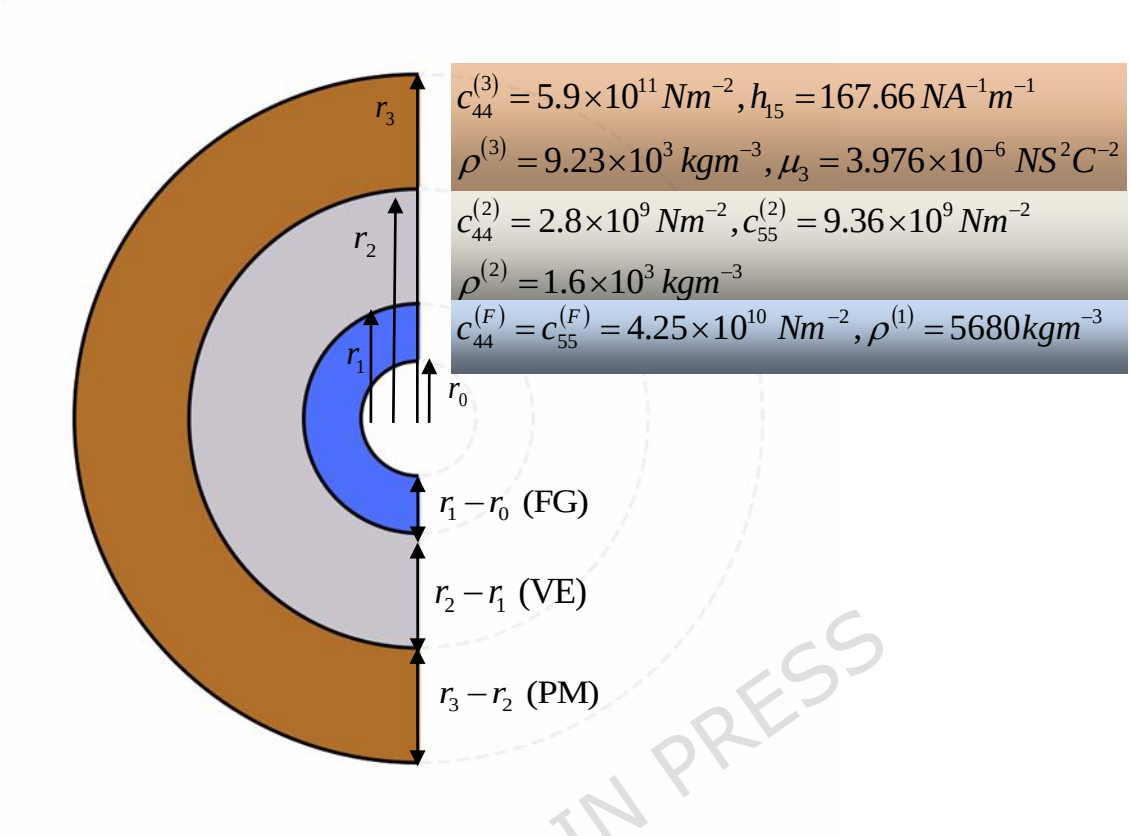


Fig. 2: Top view with data labels.

- **Layer Radii (r_0, r_1, r_2, r_3):** Chosen to reflect realistic dimensions found in advanced sensing and actuation devices, these radii establish a balanced configuration where the mechanical influence of each layer is proportionally represented.

- **Material Gradation Coefficient (l_1):** Values ranging from -1 to 0.5 were selected to capture both inverse and positive functional gradation profiles, thereby enabling an in-depth examination of how non-uniform material distribution affects wave characteristics.

- **Azimuthal Mode Numbers (n):** A set of azimuthal mode numbers, specifically n = 1, 4, and 8, was employed to analyzed the behavior of modal dispersion, encompassing both lower and higher-order wave modes

ARTICLE IN PRESS

- **Interface Imperfection Parameters (Λ_1, Λ_2):** Moderate interface imperfections were introduced with values set to 0.5. These represent realistic deviations in bonding quality and provide a basis for evaluating their role in modulating wave transmission.

- **Pre-Stress Levels (σ_θ^*):** Initial stress values of $\sigma^* = (1, 5, \text{and } 10)$ were explored to reflect different operational scenarios, from lightly stressed to significantly pre-loaded systems, common in high-performance engineering components.

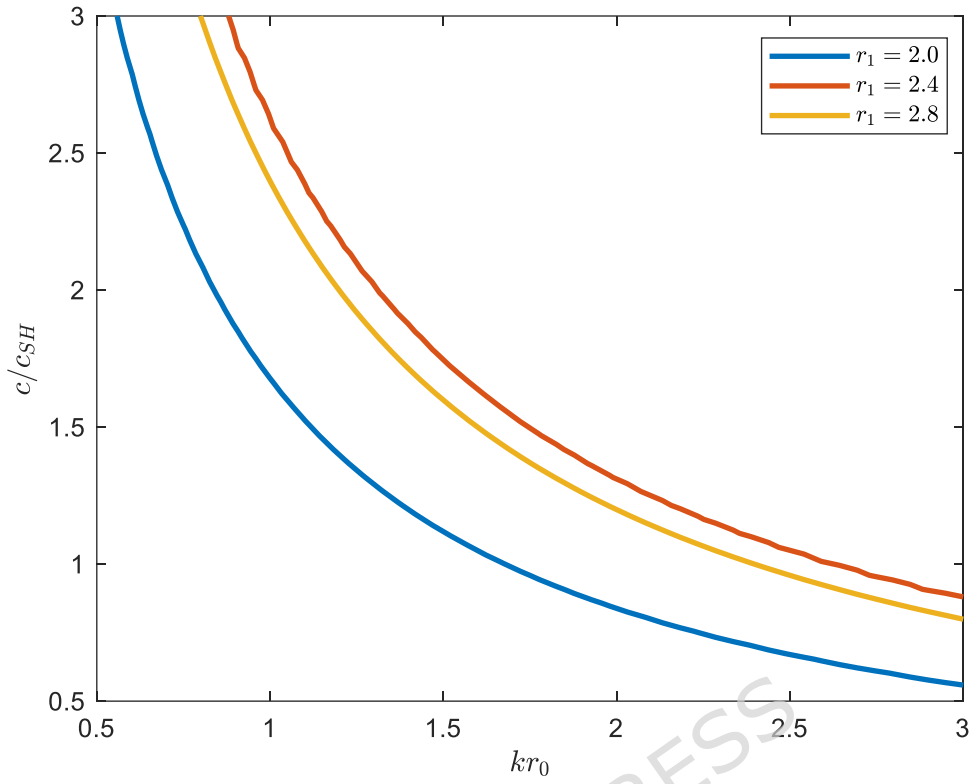
5.1 Influence of Layer Radii on Phase Velocity

This subsection investigates how the radii of individual layers within the cylindrical composite influence the propagation of circumferential SH-waves. The system consists of three concentric layers: a functionally graded (FG) orthotropic inner core, a viscoelastic (VE) damping layer, and an outer piezomagnetic (PM) shell. The variation of normalized phase velocity (c/c_{SH}) is plotted as a function of the dimensionless wavenumber (kr_0) for varying values of the respective radii: r_1 (FG), r_2 (VE), and r_3 (PM), as shown in Figs. 3(a)–3(c).

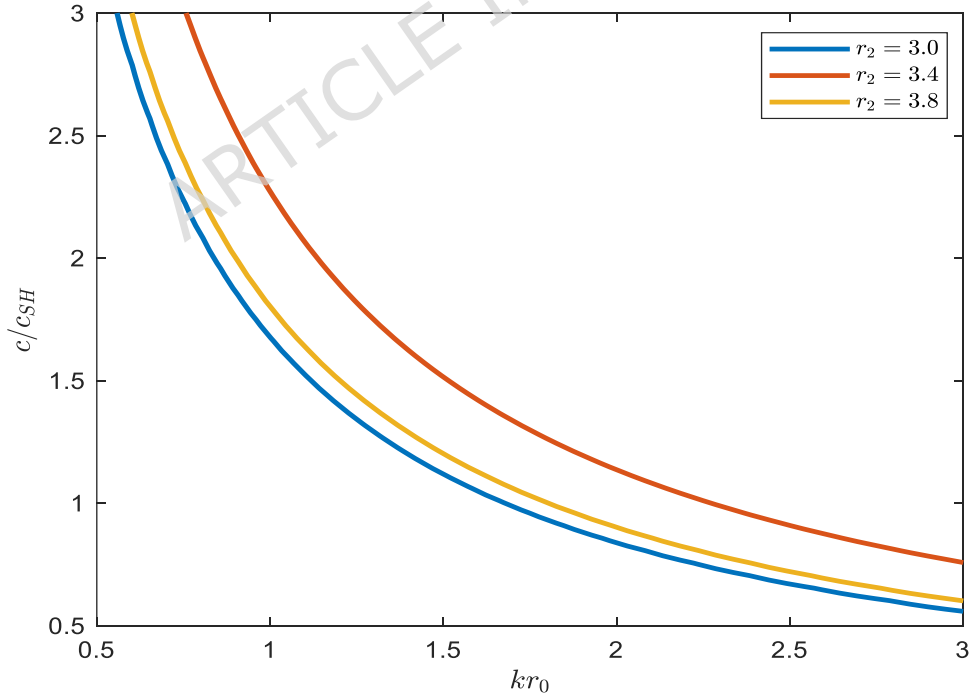
Fig. 3(a) shows how the dispersion characteristics change with different values of the inner radius $r_1 = 2.0, 2.4, 2.8$. Interestingly, the response is non-monotonic — the red curve ($r_1 = 2.4$) lies above both the blue ($r_1 = 2.0$) and yellow ($r_1 = 2.8$) curves across a large portion of the wavenumber spectrum. This indicates that an intermediate radius leads to a higher phase velocity compared to both smaller and larger radii. Such behavior arises from the radial variation of material properties in the FG layer, where wave propagation is influenced by the spatial stiffness and density distribution. An optimal radius appears to align wave energy with stiffer regions of the FG material, enhancing wave speed, whereas too small or too large a radius reduces this alignment.

Similar non-monotonic behavior is observed in Fig. 3(b), which displays the effect of the viscoelastic layer radius $r_2 = 3.0, 3.4, 3.8$. The red curve ($r_2 = 3.4$) lies above both the blue ($r_2 = 3.0$) and yellow ($r_2 = 3.8$) curves, particularly for low and moderate wavenumbers. This suggests that there exists an intermediate VE thickness that optimally balances stiffness and damping. A thinner VE layer contributes less to damping, while a thicker one may overly suppress wave speed due to enhanced energy dissipation. The peak phase velocity at $r_2 = 3.4$ reflects this trade-off between wave support and damping within the VE layer.

ARTICLE IN PRESS

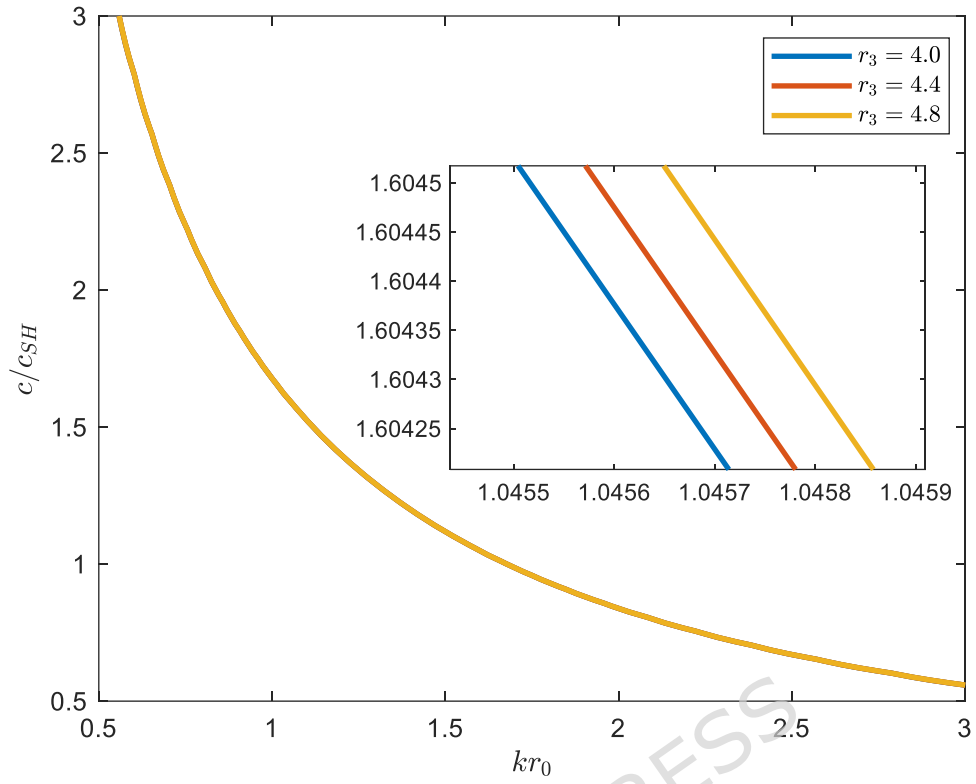


3(a)



3(b)

ARTICLE IN PRESS



3(c)

Figs. 3(a)-3(c): Phase velocity curves for different radii values versus wavenumber when $n=2$, $r_0=1$, $l_1=2$, $\Lambda_1=0.5$, $\Lambda_2=0.5$, and $\sigma^*=2$.

In contrast, Fig. 3(c) shows a monotonic trend with respect to the outer radius $r_3=4.0,4.4,4.8$. As r_3 increases, the phase velocity uniformly increases across the wavenumber range, with no curve crossing. However, the differences between curves are subtle, as highlighted in the magnified inset. This indicates that the piezomagnetic layer's effect on SH wave speed is stable and predictable, though relatively minor in the absence of active magnetic field interaction. The smooth monotonic increase suggests that increasing the PM layer thickness slightly enhances the effective stiffness of the boundary, leading to a gentle rise in phase velocity.

The analysis highlights the significant impact of each layer's geometric characteristics on wave propagation within the multilayered cylindrical system. Notably, the inner functionally graded (FG) and middle viscoelastic (VE) layers demonstrate non-linear behavior, suggesting the presence of specific radius values that optimize wave transmission. In comparison, the outer piezomagnetic (PM) layer influences phase velocity in a more consistent and linear manner. These observations underscore the potential for tuning layer thicknesses to effectively modulate the structure's dynamic performance.

ARTICLE IN PRESS

5.2 Influence of Gradation Coefficient on Phase Velocity

In Fig. 4, the dependence of normalized phase velocity c/c_{SH} on dimensionless wavenumber kr_0 is presented for various values $l_1 = -1, 0, 0.5$ of the material gradation coefficient, which governs the variation of mechanical properties within the FG inner layer. This parameter effectively tunes the spatial distribution of stiffness and density along the radial direction

The red curve corresponds to $l_1 = 0$, representing a homogeneous FG layer with uniform material properties. The blue curve depicts $l_1 = -1$, indicating inverse gradation—where material stiffness increases toward the inner radius. The yellow curve shows the case $l_1 = 0.5$, representing a positive gradation, with increasing stiffness and density outward toward the FG layer's outer boundary. Across the entire wavenumber range, it is evident that positive gradation ($l_1 = 0.5$) results in the highest phase velocity, while homogeneous material ($l_1 = 0$) yields the lowest, and inverse gradation ($l_1 = -1$) lies in between. This trend is further confirmed by the magnified inset, which highlights subtle but consistent separations between the three curves.

The observed differences arise from how the radial gradation profile aligns with wave energy concentration. In the case of positive gradation, stiffer material near the outer surface enhances wave speed, as SH-waves are more responsive to outer-layer stiffness. In contrast, inverse gradation concentrates stiffness near the inner radius, which is less influential for circumferential SH-waves, resulting in a slightly reduced phase velocity.

Moreover, the spacing between the curves is non-uniform, and this is not accidental. It reflects the nonlinear effect of the gradation parameter on the mechanical response of the FG layer. Changes in l_1 do not produce proportionally linear shifts in stiffness distribution. As a result, the impact on phase velocity increases disproportionately, especially in the positive gradation direction where outer regions where SH-wave energy is more active contribute more effectively to wave propagation. This asymmetric sensitivity makes positive gradation significantly more effective in enhancing wave speed than inverse gradation is in reducing it.

In conclusion, the gradation parameter l_1 plays a pivotal role in tailoring SH-wave dispersion by spatially redistributing mechanical properties. Positive gradation enhances phase velocity by aligning stiffer material with dominant wave energy regions, while inverse gradation offers a moderate reduction. This finding reinforces the utility of functional

ARTICLE IN PRESS

gradation as a tunable design tool for optimizing dynamic performance in advanced cylindrical structures.

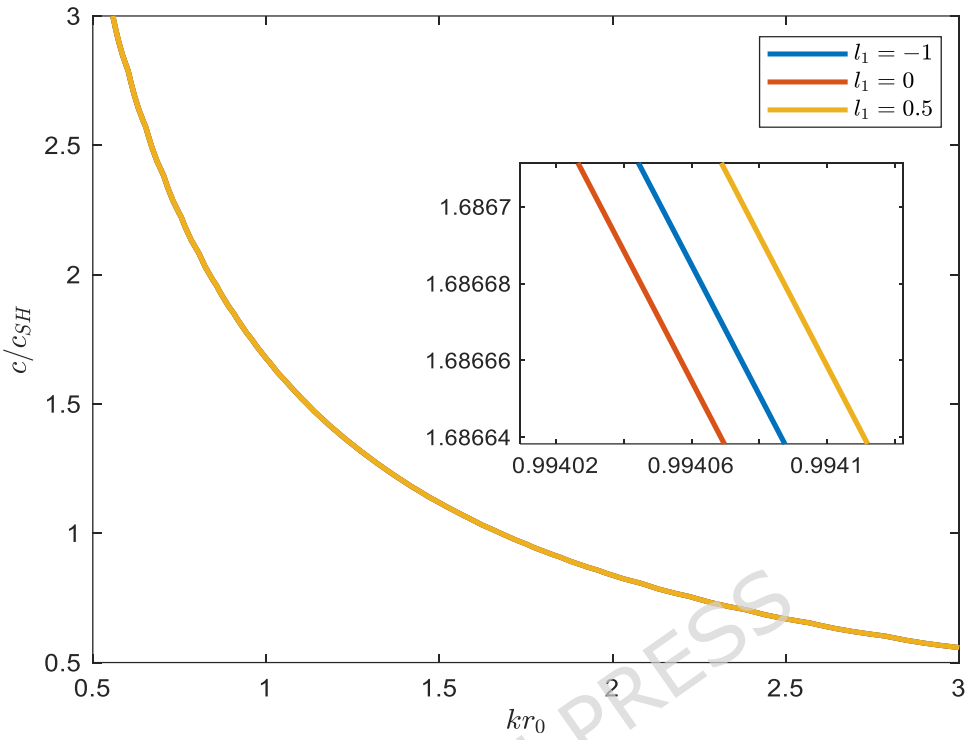


Fig. 4: Phase velocity curves for different l_1 values versus wavenumber when $n=2$, $r_0=1$, $r_1=2$, $r_2=3$, $r_3=4$, $\Lambda_1=0.5$, $\Lambda_2=0.5$, and $\sigma^*=2$.

5.3 Influence of Angular Mode on Phase Velocity

Fig. 5 illustrates the variation of normalized phase velocity (c/c_{SH}) with respect to the dimensionless wave number (kr_0) for different angular mode numbers ($n=1,4,8$). The angular mode number (n) characterizes the number of circumferential wave cycles around the cylindrical geometry and directly influences the wave's angular structure.

Across all modes, a consistent trend is observed wherein the normalized phase velocity decreases as the dimensionless wavenumber increases, indicative of dispersive SH-wave behavior. However, the variation in phase velocity with increasing n is distinctly nonlinear**.** The lowest angular mode ($n=1$) exhibits the highest phase velocity across the entire range of wavenumbers shown. As the angular mode number increases from $n=1$ to $n=4$, a pronounced and rapid decline in phase velocity is observed. The $n=4$ mode (red curve) shows considerably lower velocities compared to the $n=1$ mode, especially at lower wavenumbers. Further increasing the angular mode number from $n=4$ to $n=8$ results in a

ARTICLE IN PRESS

smaller, less pronounced decrease in phase velocity. The $n=8$ mode (yellow curve) is closer to the $n=1$ curve than the $n=4$ curve, particularly at higher wave numbers.

This behavior suggests that the influence of the angular mode number on phase velocity does not scale linearly. The transition from lower to moderate modes introduces a stronger shift in wave dynamics than the jump from moderate to higher modes. Physically, higher n values correspond to more tightly confined waveforms around the circumference, which increases the effective inertia and reduces the propagation speed. However, after a certain point (as seen between $n=1$ and $n=8$), this effect saturates, and the curves tend to converge, especially at larger wavenumbers.

In conclusion, the angular mode number n plays a crucial and nonlinearly scaling role in SH wave propagation. Lower modes are associated with faster and more stable wave transmission, while higher modes introduce sharp velocity drops that eventually level off, reflecting a saturation effect in the modal influence on dispersive behavior. This trend emphasizes the critical role of the mode number in analyzing wave behavior within cylindrical structures, especially when precise control over wave velocity is required for targeted applications.

ARTICLE IN PRESS

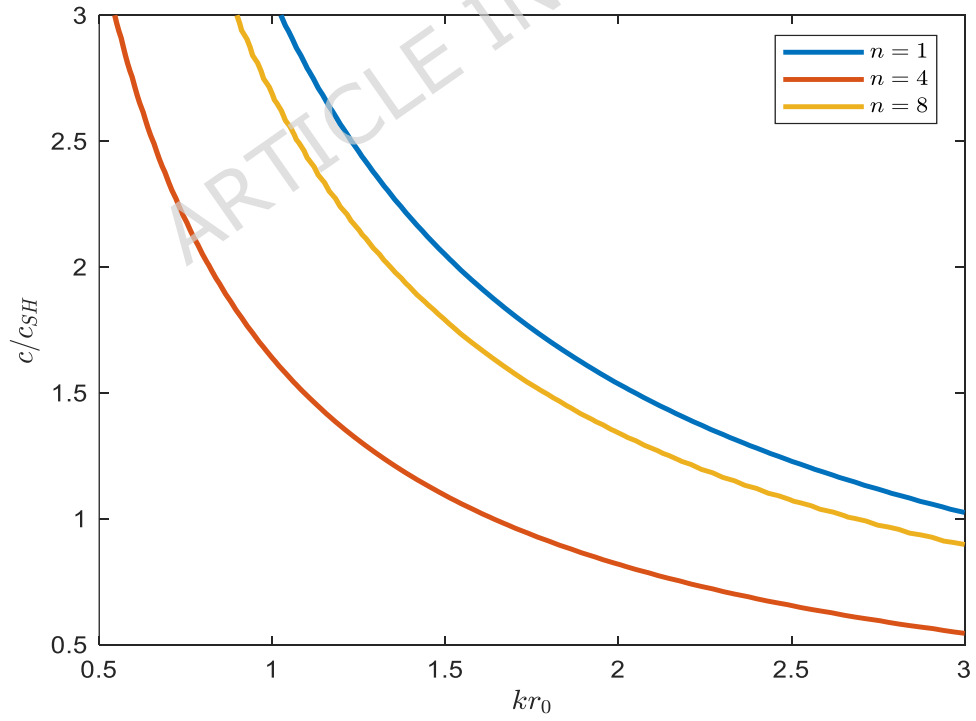


Fig. 5: Phase velocity curves for different n values versus wavenumber when $l_1=2$, $r_0=1$, $r_1=2$, $r_2=3$, $r_3=4$, $\Lambda_1=0.5$, $\Lambda_2=0.5$, and $\sigma^*=2$.

ARTICLE IN PRESS

5.4 Influence of Material Gradation Coefficient on Stress Distribution

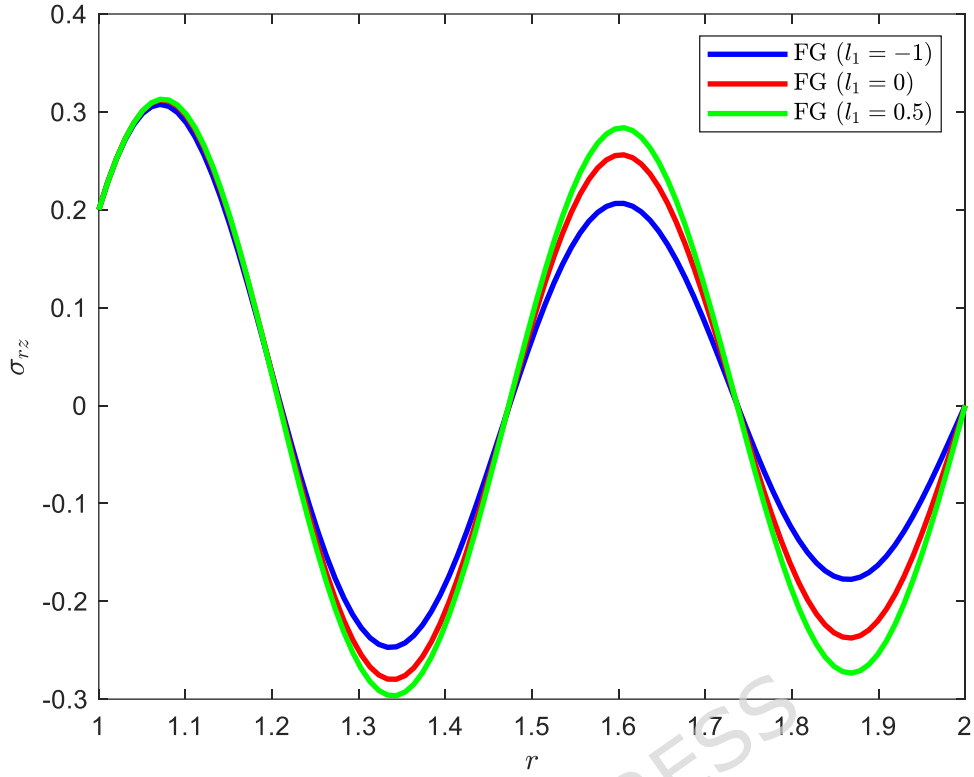
Fig. 6(a) presents the variation of shear stress σ_{rz} in the Functionally Graded (FG) material for different values of the gradation parameter l_1. The stress profile exhibits smooth oscillatory behavior within a moderate range (approximately -0.3 to 0.4). Both positive and negative shear stresses are observed, with symmetry about the mid-radius, indicating a balanced shear response within the FG layer. As the gradation parameter increases from $l_1 = -1$ to $l_1 = 0.5$, the amplitude of oscillations becomes slightly more pronounced. This reflects the effect of enhanced material heterogeneity, where a higher gradation introduces increased stiffness variation across the radius, thereby affecting the shear wave interaction. The nonzero starting value of shear stress at the inner boundary confirms the influence of externally applied mechanical loading in the second boundary condition set, as formulated in the surface response analysis 4.2.

Fig. 6(b) illustrate the shear stress σ_{rz} in the Viscoelastic (VE) material. The stress magnitude is significantly smaller (around 10^{-2}) and shows mild oscillatory behavior with damped amplitude, consistent with the energy-absorbing nature of viscoelastic materials. The response becomes more reactive with increasing l_1, as stronger gradients in the FG layer induce higher stress transmission into the VE material.

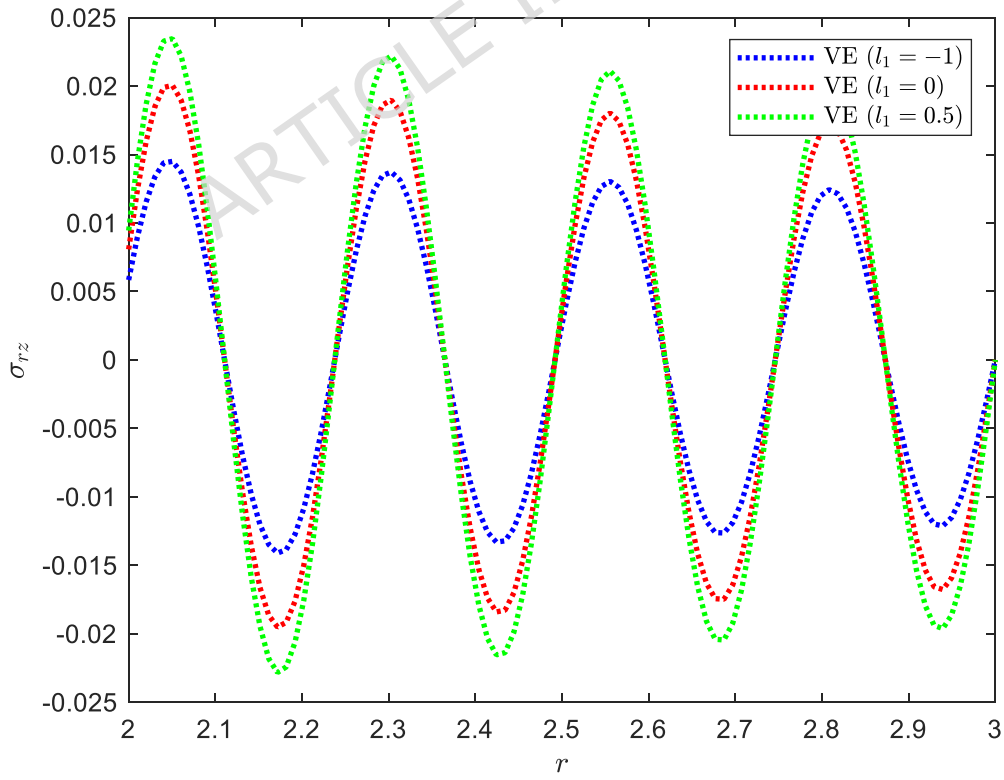
Fig. 6(c) depicts the radial stress σ_{rz} in the Piezomagnetic (PM) material. The stress magnitudes are minimal (around 10^{-5}) and gradually reduce toward the free surface at $r = 4$, where the stress correctly vanishes, fulfilling the outer boundary condition. The influence of l_1 is weak but noticeable higher values slightly elevate the internal stress within the PM region as a result of enhanced interfacial coupling with the VE layer. The smooth decay confirms the magneto-mechanical character of the PM material, which plays a secondary mechanical role.

Fig. 6(d) presents the combined stress profiles of the three constituent medium layers to highlight the complete stress distribution within the composite system. The FG layer shows the highest stress amplitudes with oscillatory transitions, smoothly transmitting into the VE layer, which then decays into negligible stress in the PM layer. The boundaries at $r = 2$, $r = 3$, and $r = 4$ exhibit stress continuity, affirming correct application of boundary and interface conditions. The stress transmission from FG through VE into PM reflects the balance of stiffness, damping, and field coupling effects across the composite.

ARTICLE IN PRESS

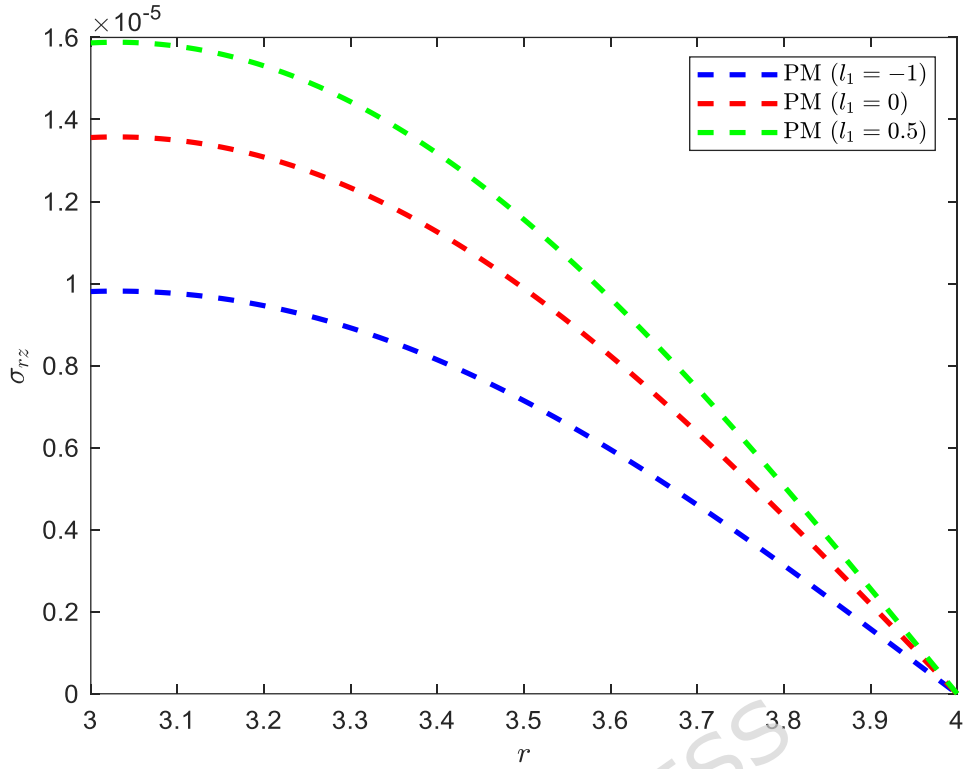


6(a)

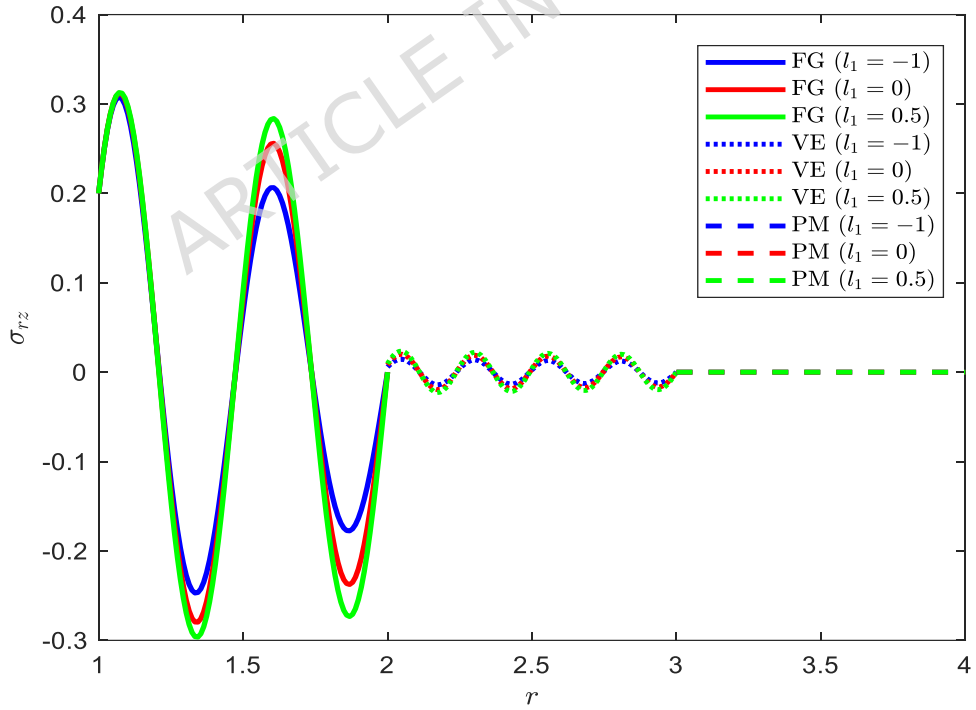


6(b)

ARTICLE IN PRESS



6(c)



6(d)

Figs. 6(a)-6(d): Stress distribution curves for different l_1 values versus radius when $n=2$, $r_0=1$, $r_1=2$, $r_2=3$, $r_3=4$, $\Lambda_1=0.5$, $\Lambda_2=0.5$, $\sigma^*=2$ and $\sigma_{ext}=0.2$.

ARTICLE IN PRESS

The gradation parameter l_1 significantly influences the stress distribution throughout the layered structure. As l_1 increases, the stress profile becomes more uniform across the layers, effectively reducing localized stress concentrations and improving the structure's overall mechanical integrity. Conversely, lower values tend to cause localized stress build-up, particularly near the interfaces, which may compromise structural stability. By tuning l_1, the material properties can be precisely tailored to optimize both load-bearing capacity and functional performance.

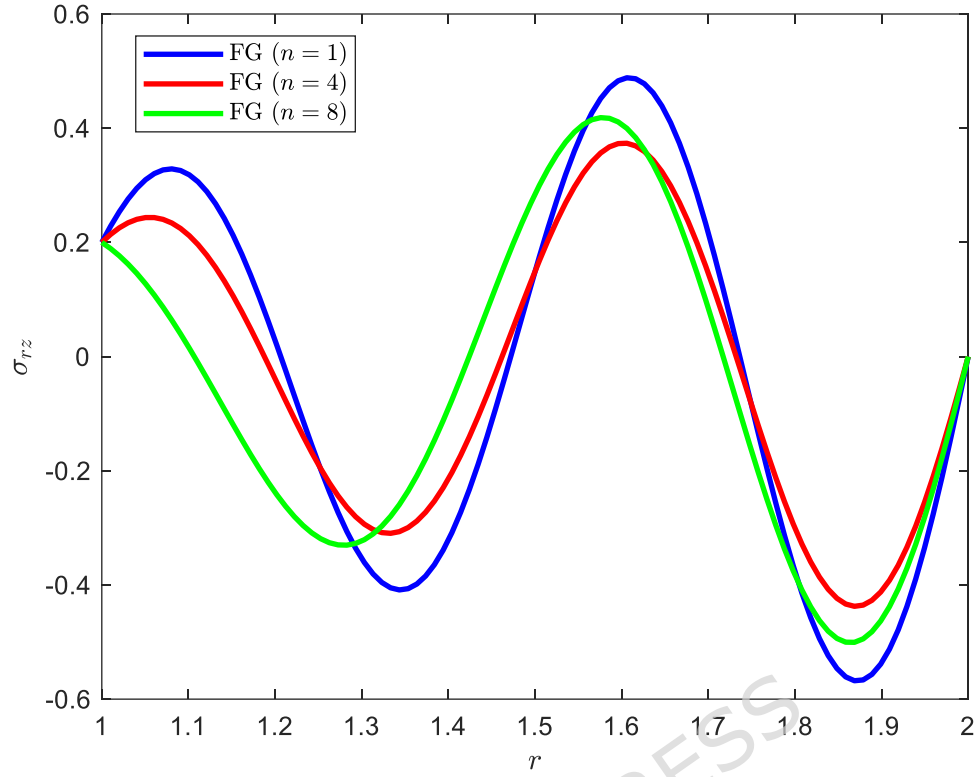
5.5 Influence of Azimuthal Mode on Stress Distribution

The angular variation of SH-wave propagation, dictated by the circumferential wave number n, has a pronounced impact on the stress distribution within the cylindrical composite structure. The stress profiles reveal that each layer exhibits a distinct response to these wave dynamics, reflecting the influence of their individual material properties.

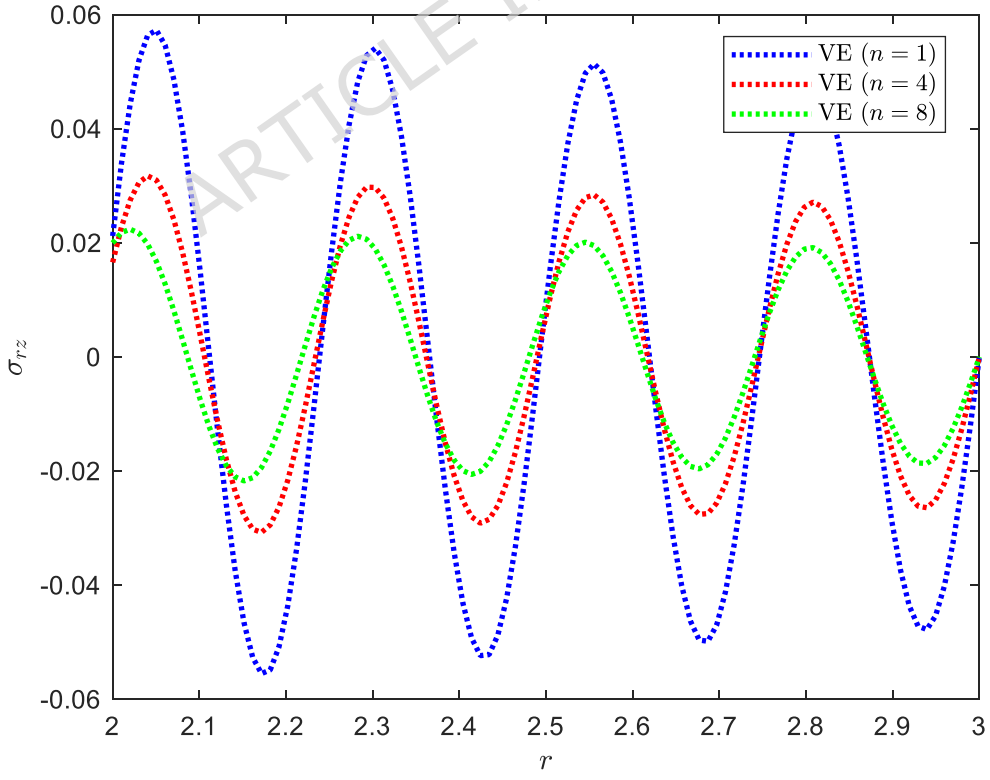
In the functionally graded (FG) layer, the stress exhibits periodic oscillations with relatively large amplitudes, varying approximately between -0.6 and 0.6, as illustrated in Fig. 7(a). The frequency of these oscillations is closely tied to the mode number n; higher n values lead to more rapid fluctuations in the stress pattern. The FG layer displays gradual transitions between compressive and tensile regions, suggesting that the material gradation contributes to a smooth and balanced stress distribution without sharp discontinuities. This uniform distribution arises from the gradual variation of mechanical properties across the layer, promoting structural stability and mitigating stress concentrations under dynamic loading.

The viscoelastic (VE) material layer demonstrates significantly lower stress magnitudes, approximately ranging from -0.06 and 0.06, as illustrated in Fig. 7(b). Although the stress levels are diminished relative to the FG layer, the angular variation persists, manifested through periodic oscillations with noticeably smaller amplitudes. The damping characteristics inherent to viscoelastic materials contribute to smoother stress profiles and attenuate stress peaks, reflecting the VE layer’s capacity to absorb and dissipate vibrational energy. This behavior is crucial in applications where vibration mitigation and damping are essential for structural integrity and performance.

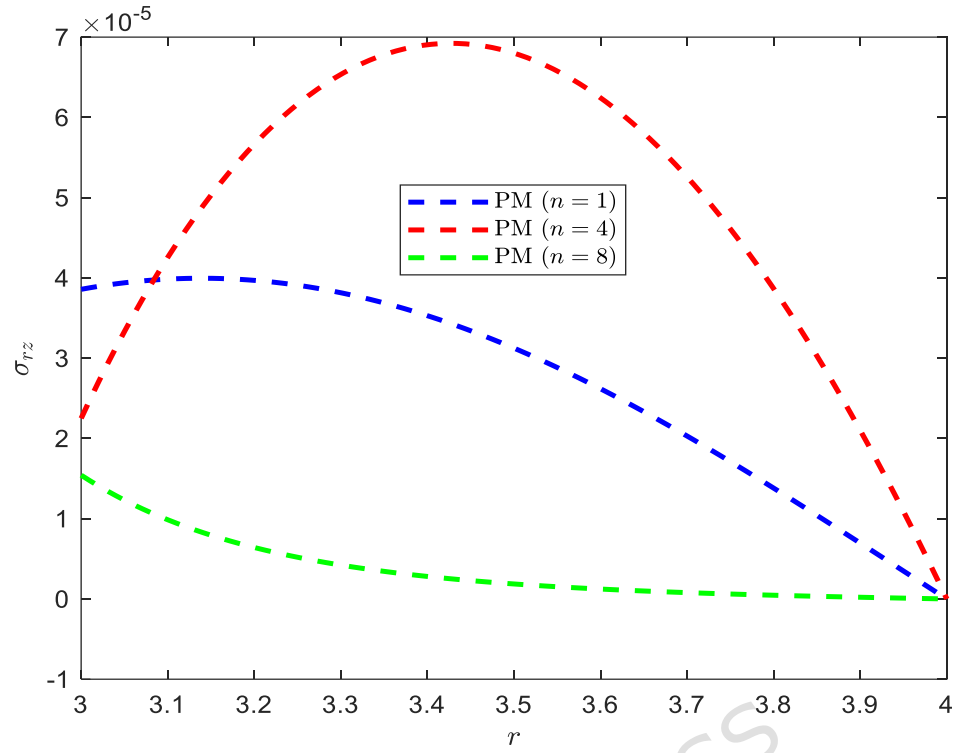
ARTICLE IN PRESS



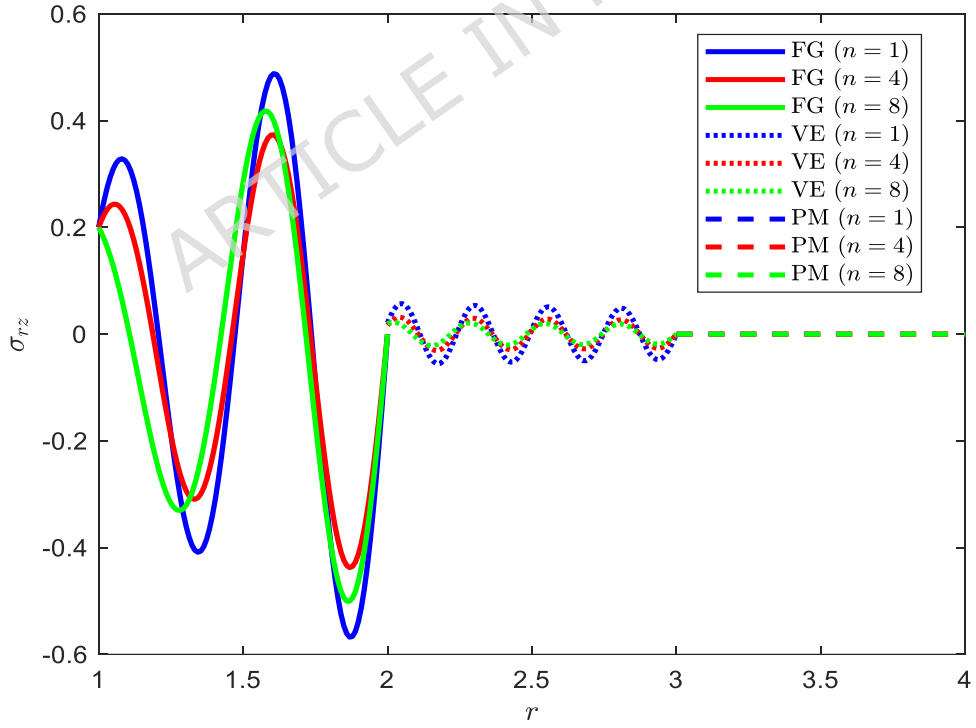
7(a)



7(b)



7(c)



7(d)

Figs. 7(a)-7(d): Stress distribution curves for different n values versus radius when $l_1 = 3$, $r_0 = 1$, $r_1 = 2$, $r_2 = 3$, $r_3 = 4$, $\Lambda_1 = 0.5$, $\Lambda_2 = 0.5$, $\sigma^* = 2$ and $\sigma_{ext} = 0.2$.

ARTICLE IN PRESS

In contrast, the piezomagnetic (PM) material layer displays a significantly different stress response, with magnitudes on the order of 10^{-5}, as observed in the Fig. 7(c). The stress in the PM layer varies more gradually, lacking the pronounced oscillations seen in the FG and VE layers. Instead, it exhibits a smoother, broad peak or gradual decay, depending on the angular mode. The lower stress levels are typical of piezomagnetic media, where the coupling between mechanical stress and magnetic fields can lead to redistribution or attenuation of localized mechanical forces. Such behavior is advantageous in applications involving magneto-mechanical coupling, where stability and low mechanical stress levels are essential for precise functional responses.

Fig. 7(d) presents a holistic depiction of stress propagation across the composite system. The PM and VE layers demonstrate moderate and relatively uniform stress responses, whereas the FG layer is subject to considerably higher stress magnitudes. This contrast highlights the unique functional contributions of each layer: the FG layer provides mechanical strength and stiffness; the VE layer contributes damping and energy dissipation; and the PM layer enables magneto-mechanical interactions with minimal stress fluctuations.

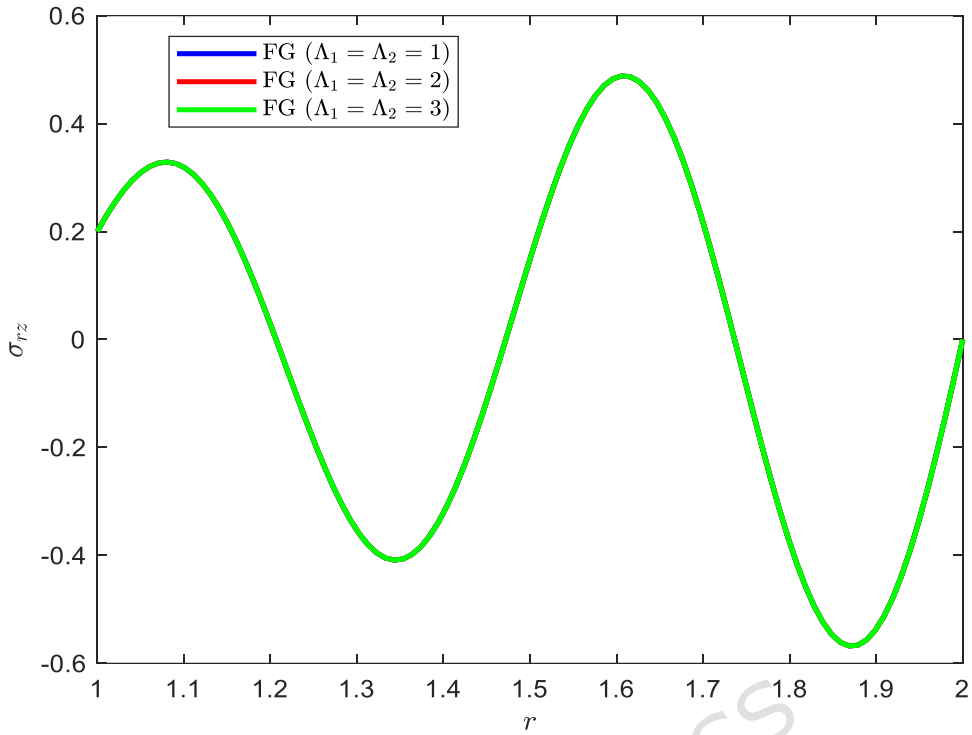
Overall, the influence of the angular mode n is evident in all layers, introducing periodic variations in stress profiles whose frequency and amplitude depend on the material properties. Higher n values lead to more frequent oscillations, with the FG layer showing the most pronounced changes due to its stiffness and material gradient. In contrast, the VE and PM layers moderate these variations through damping or magneto-mechanical coupling, contributing to the overall structural performance and functional versatility of the composite cylindrical system.

ARTICLE IN PRESS

5.6 Influence of Imperfection Parameters on Stress Behavior

The focus of this section is on analyzing the stress behavior of the layered cylindrical composite system subjected to interfacial discontinuities, modeled via the normalized imperfection parameters Λ_1 and Λ_2, which encapsulate deviations from perfect mechanical bonding at the inner and outer interfaces, respectively. These imperfections serve as critical indicators of interface compliance and their impact on stress transmission across the layers.

ARTICLE IN PRESS

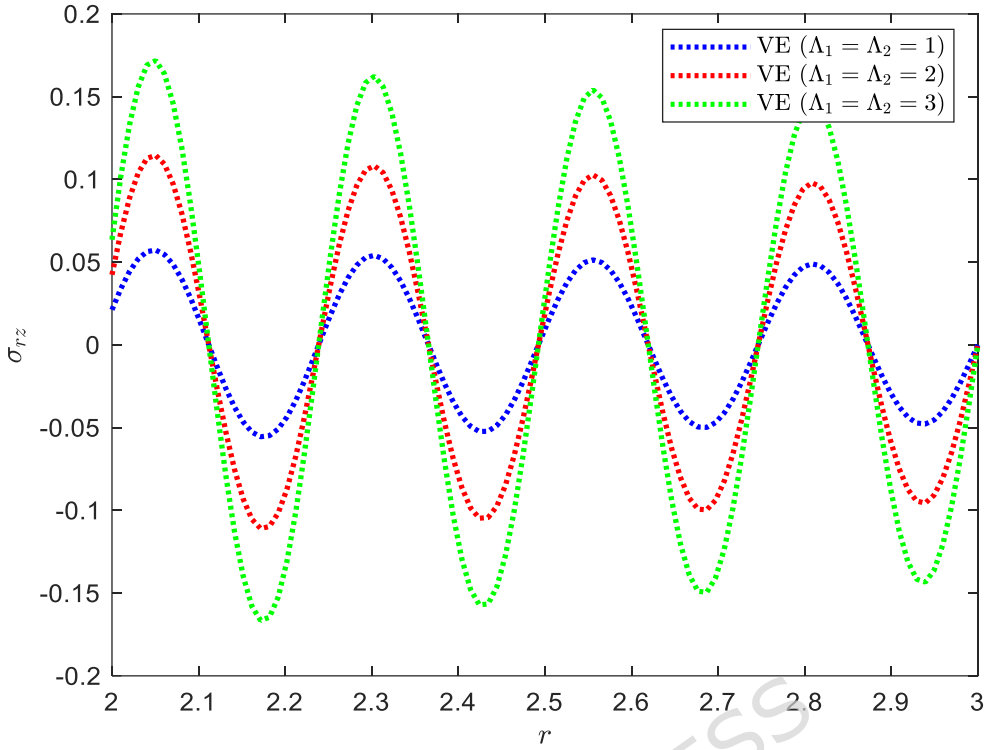


8(a)

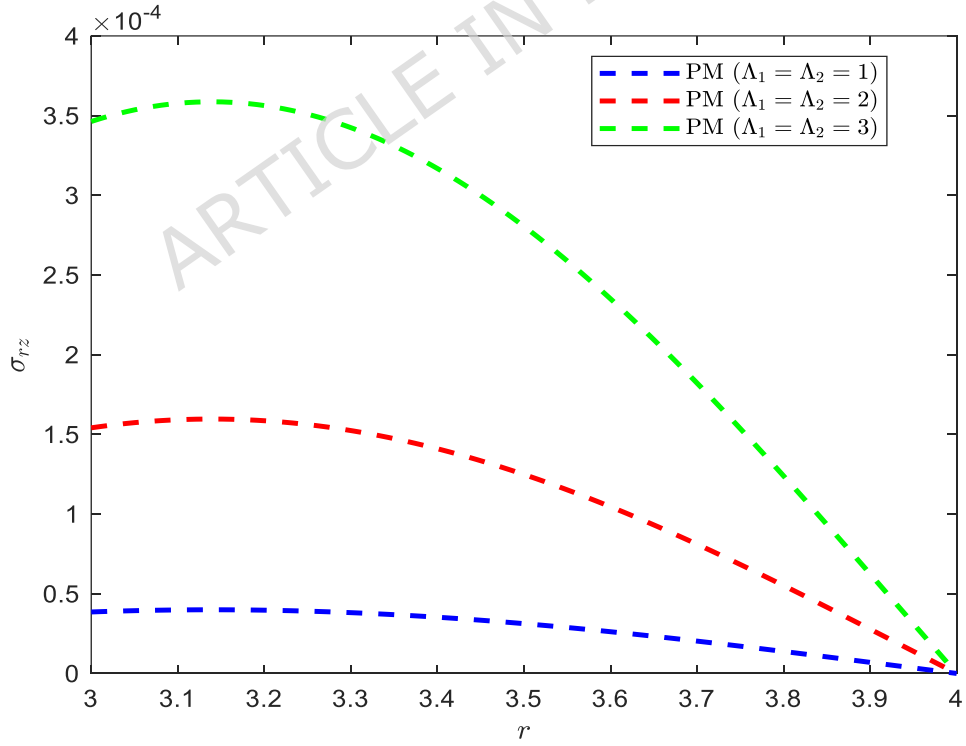
As shown in Fig. 8(a), the FG layer displays a relatively smooth stress response for various equal values of the imperfection parameters Λ_1 and Λ_2, even in the presence of discontinuities at its interface with the VE layer. This behavior suggests that the graded material composition effectively dissipates localized stress disturbances, preventing

ARTICLE IN PRESS

ARTICLE IN PRESS

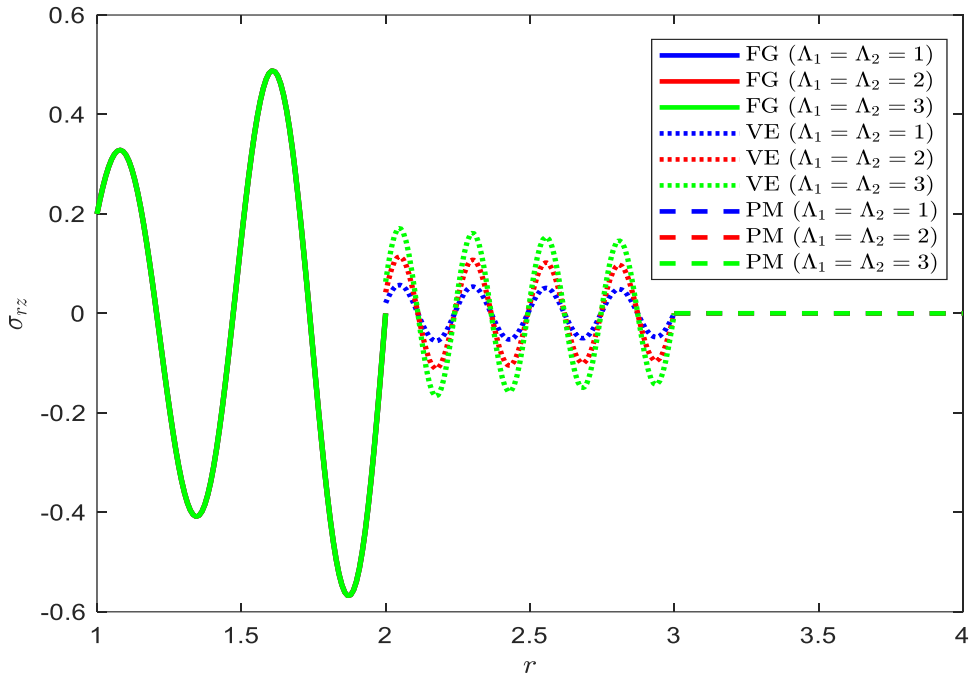


8(b)



8(c)

ARTICLE IN PRESS



8(d)

Figs. 8(a)-8(d): Stress distribution curves for different Λ_1 and Λ_2 values versus radius when $n=2$, $l_1=3$ $r_0=1$, $r_1=2$, $r_2=3$, $r_3=4$, $\sigma^*=2$ and $\sigma_{ext}=0.2$.

significant stress peaks or abrupt changes. Consequently, even as the imperfection parameters increase, the FG layer continues to transmit stress toward the adjacent VM layer without severe disruptions.

Fig. 8(b) presents the stress distribution profile within the VE medium, highlighting its mechanical response under SH-wave excitation. Compared to the FG layer, the VE layer is noticeably more responsive to variations in interfacial imperfections. Changes in Λ_1 and Λ_2 result in visible adjustments in the stress near both interfaces. Nevertheless, the stress curve remains continuous, indicating that the VE layer retains its role as a mechanical intermediary between the FG and PM layers. Localized stress alterations caused by imperfections remain within moderate bounds, ensuring that the layer's mechanical robustness is preserved.

Fig. 8(c) presents the stress profile within the PM medium, where imperfections at the VE/PM interface lead to subtle fluctuations in stress close to the boundary. However, stress levels throughout the PM layer remain quite low, consistent with its function in bearing minimal mechanical loads. A progressive reduction in stress is observed as one moves toward the outer boundary, reflecting the effect of the stress-free boundary condition. Overall, the

ARTICLE IN PRESS

influence of Λ_1 and Λ_2 remains marginal, maintaining a smooth and stable stress distribution within the PM layer and thereby preserving its magneto-mechanical functionality.

Fig. 8(d) displays the consolidated stress distribution profiles across all three layers, highlighting the impact of varying imperfection parameters at the interfaces. Minor discontinuities or shifts in stress appear at the interfaces where Λ_1 and Λ_2 have nonzero values. Nonetheless, these perturbations remain modest in magnitude, and the stress retains continuity throughout the entire structure. This indicates that irrespective of interfacial mechanical imperfections, the system is capable of maintaining structural cohesion and effective stress transfer across layers.

5.7 Influence of initial stress on stress distribution

The influence of initial stress $\sigma*$ $(1,5,10)$ on the stress distribution within the multilayered structure is explored in Figs. 9(a)–9(d).

In Fig. 9(a), the FG layer is shown to maintain a largely stable stress profile regardless of changes in initial stress. Although this layer does not directly experience the imposed initial stress, subtle modifications can arise due to mechanical interactions with the adjacent VE layer, where stress transmission across the interface may slightly alter the FG region's behavior.

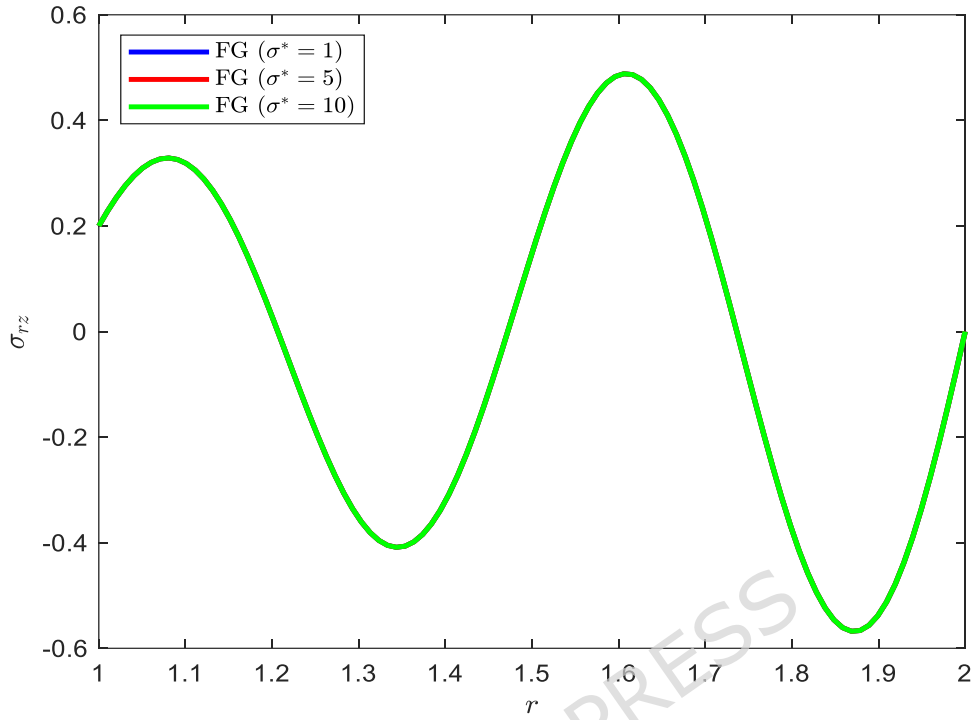
Turning to Fig. 9(b), the VE medium serves as a mechanical bridge between the FG and PM mediums. Variations in initial stress within the PM layer subtly influence the VE layer through interfacial conditions, yet the stress distribution in the VE region remains nearly unchanged overall, indicating its resilience to indirect stress effects.

Fig. 9(c) focuses on the PM layer, where the impact of initial stress becomes pronounced. Across the radial span from $r=3$ to $r=4$, stress values decrease steadily, with higher values of σ^* leading to a more significant drop. For instance, when $\sigma^*=1$, the stress remains relatively high, while larger values such as $\sigma^*=5$ and $\sigma^*=10$ cause a faster reduction. This suggests that although elevated initial stress contributes to reducing peak stress levels and potential mechanical failure risks, it may simultaneously suppress strain levels, which are essential for achieving optimal magneto-mechanical performance in applications like actuators and sensors.

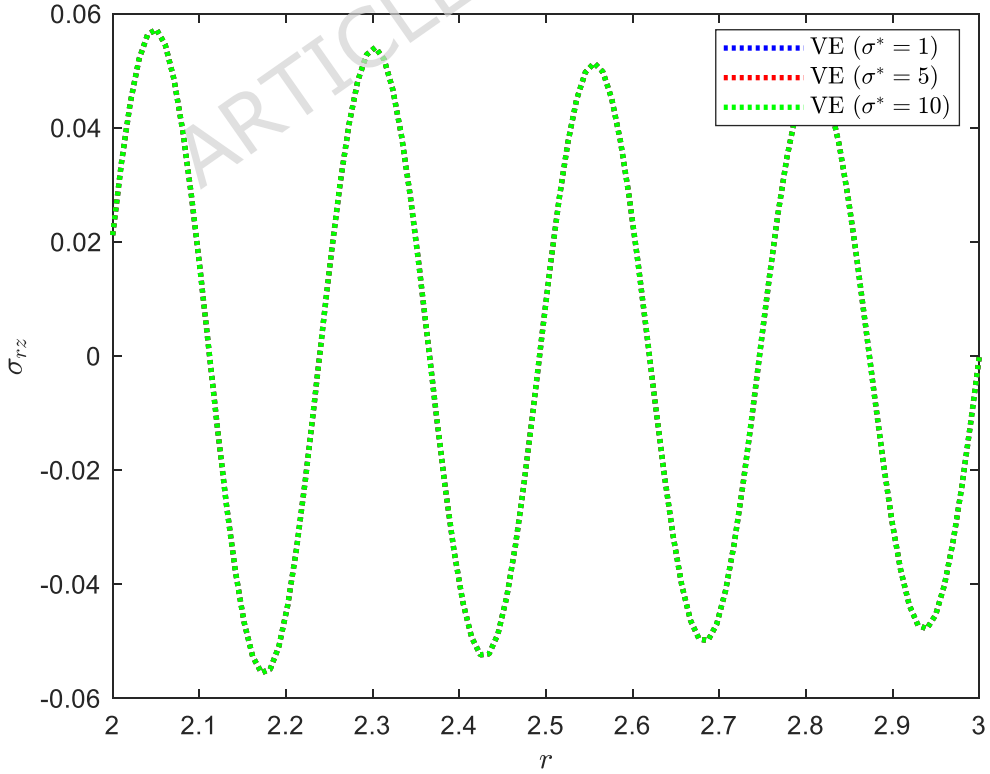
The overall stress response of the composite structure, accounting for different initial stress values in the PM layer, is depicted in Fig. 9(d). Introducing tensile initial stress into the PM layer redistributes the overall stress profile, shifting stresses toward lower magnitudes

ARTICLE IN PRESS

throughout the multilayered system. This redistribution can enhance mechanical stability but may also influence functional performance depending on the application.

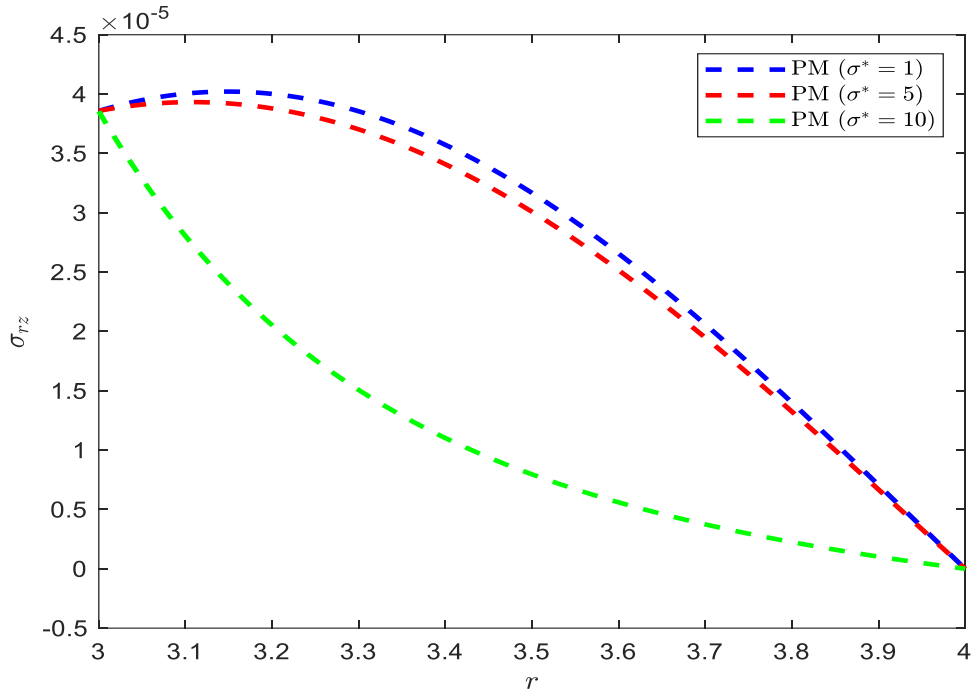


9(a)

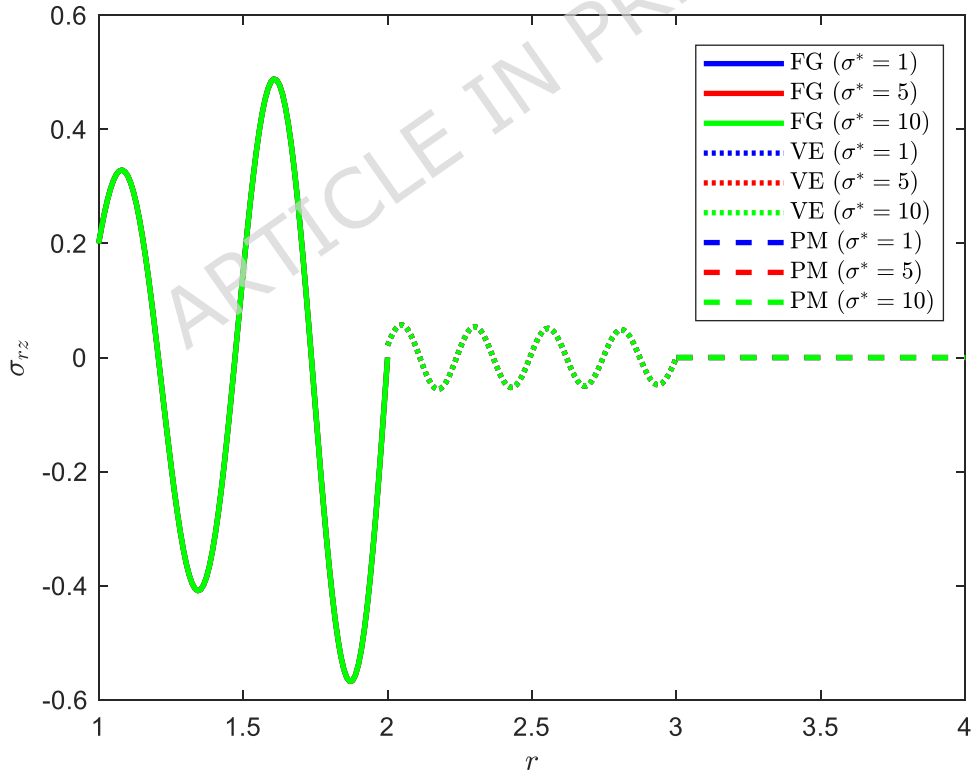


9(b)

ARTICLE IN PRESS



9(c)



9(d)

Figs. 9(a)-9(d): Stress distribution curves for different σ^* values versus radius when $n=2$, $l_1=3$, $r_0=1$, $r_1=2$, $r_2=3$, $r_3=4$, $\Lambda_1=0.5$, $\Lambda_2=0.5$, and $\sigma_{ext}=0.2$.

ARTICLE IN PRESS

6. Conclusion

This study presents a comprehensive investigation into the propagation of circumferential SH-waves in a three-layered cylindrical composite system incorporating FG, VE, and PM materials. Emphasizing the effects of mechanical imperfections, material gradation, and initial stresses, the analysis has yielded valuable insights into the wave dynamics and stress behavior crucial for magneto-mechanical applications. Based on these findings, the following conclusions can be drawn:

- The inner FG layer and middle VM layer exhibit non-monotonic influence on phase velocity, pointing to the presence of optimal radii where wave propagation is most efficient.
- The phase velocity exhibits a nonlinear and asymmetric response to the gradation parameter l_1. Positive gradation ($l_1 = 0.5$) yields the highest velocity, inverse gradation ($l_1 = -1$) gives a moderate increase, while the homogeneous case ($l_1 = 0$) results in the lowest velocity—highlighting the strong influence of outward stiffness distribution on wave propagation.
- The phase velocity exhibits a nonlinear dependence on the angular mode number n; a sharp drop is observed from low to moderate modes, while higher modes show diminishing variation, indicating a saturation effect in wave speed reduction at large n.
- The material gradation parameter significantly influences stress distribution across the layered structure, with higher values promoting more uniform stress profiles and minimizing concentrations, thereby allowing precise tailoring of material properties for optimized load-bearing capacity and functional performance.
- The angular mode number significantly influences stress distribution across all composite layers, introducing periodic variations whose frequency and amplitude are governed by the mode number and material properties, with the FG layer showing the most pronounced oscillations and the VE and PM layers moderating these variations through damping or magneto-mechanical coupling.
- Initial stress primarily impacts the PM layer by reducing its stress levels, which in turn subtly redistributes stress throughout the entire multilayered system, enhancing mechanical stability but potentially affecting electro-mechanical performance by suppressing strain.

ARTICLE IN PRESS

The complex interplay of material gradation, angular mode number, initial stress, and interface imperfections plays a pivotal role in shaping the wave propagation characteristics and stress distribution throughout the multilayered cylindrical system. Recent studies on cylindrical shell systems demonstrate their importance in spacecraft structures, nanoscale biological modeling, and artificial gravity simulations [57], [58], [59], [60]. The proposed tri-layered model therefore provides a theoretical framework applicable to advanced multifunctional shell structures.

Acknowledgment

Authors are also sincerely thankful to Amrita Vishwa Vidyapeetham, Mysuru campus, India and Gurugram University, India for supporting immensely by providing great opportunity, guidance, best facilities and equipments.

Funding

There is no funding for this research

Author Credit Statement

Vipin Gupta: Supervision, Methodology. **Aymen Flah:** Conceptualization, Investigation**.** **Murat Yaylacı**: Formal analysis, Validation, Resources. **Abhik Sur:** Visualization, Writing – review & editing. **Ivo Pergl:** Software. **Mohammad Ghatasheh:** Writing – review & editing. **Soumik Das:** Visualization, Software, Writing – original draft.

Declaration of interest

The authors declare that they have no known competing financial interests or personal relationships that could have appeared to influence the work reported in this paper.

Declaration of generative AI use

This statement confirms that the authors did not use AI in the core process

Data Availability Statement

All data generated or analyzed during this study are included in this published article.

Appendix

The non-zero entries of the matrix $\Upsilon = [\Upsilon_{uv}]$, $X = [X_{u1}]$, and $Q = [Q_{u1}]$; $u, v = 1-8$ are given below

ARTICLE IN PRESS

$$\Upsilon_{11}=r_0^{-l_1/2}c_{44}^{(F)}\left[-\frac{l_1}{2r_1}J_p\left(\frac{r_0\omega}{\beta_1}\right)+J_{p,r}\left(\frac{r_0\omega}{\beta_1}\right)\right],\ \Upsilon_{12}=r_0^{-l_1/2}c_{44}^{(F)}\left[-\frac{l_1}{2r_1}Y_p\left(\frac{r_0\omega}{\beta_1}\right)+Y_{p,r}\left(\frac{r_0\omega}{\beta_1}\right)\right]$$

$$\Upsilon_{25}=c_{44}^{(3)}J_{p,r}\left(r_3\xi\right)+\frac{h_{15}^2}{\mu_3}J_{p,r}\left(r_3\xi\right),\ \ \Upsilon_{26}=c_{44}^{(3)}Y_{p,r}\left(r_3\xi\right)+\frac{h_{15}^2}{\mu_3}Y_{p,r}\left(r_3\xi\right),\ \Upsilon_{27}=-nh_{15}r_3^{-n-1},$$

$$\Upsilon_{28}=nh_{15}r_3^{n-1},\ \Upsilon_{31}=r_1^{-l_1/2}c_{44}^{(F)}\left[-\frac{l_1}{2r_1}J_p\left(\frac{r_1\omega}{\beta_1}\right)+J_{p,r}\left(\frac{r_1\omega}{\beta_1}\right)\right],$$

$$\Upsilon_{32}=r_1^{-l_1/2}c_{44}^{(F)}\left[-\frac{l_1}{2r_1}Y_p\left(\frac{r_1\omega}{\beta_1}\right)+Y_{p,r}\left(\frac{r_1\omega}{\beta_1}\right)\right],\ \Upsilon_{33}=-\bar{c}_{44}^{(2)}J_{p,r}\left(\frac{r_1\omega}{\beta_2}\right),\ \Upsilon_{34}=-\bar{c}_{44}^{(2)}Y_{p,r}\left(\frac{r_1\omega}{\beta_2}\right),$$

$$\Upsilon_{41}=\gamma^{(1,2)}J_p\left(\frac{r_1\omega}{\beta}\right)r_1^{-l/2},\ \Upsilon_{42}=\gamma^{(1,2)}Y_p\left(\frac{r_1\omega}{\beta}\right)r_1^{-l/2}$$

$$\Upsilon_{43}=\left[\bar{c}_{44}^{(2)}J_{p,r}\left(\frac{r_1\omega}{\beta_2}\right)-\gamma^{(1,2)}J_p\left(\frac{r_1\omega}{\beta_2}\right)\right],\ \Upsilon_{44}=\left[\bar{c}_{44}^{(2)}Y_{p,r}\left(\frac{r_1\omega}{\beta_2}\right)-\gamma^{(1,2)}Y_p\left(\frac{r_1\omega}{\beta_2}\right)\right]$$

$$\Upsilon_{51}=\frac{h_{15}}{\mu_3}J_p\left(r_2\xi\right),\ \Upsilon_{52}=\frac{h_{15}}{\mu_3}J_p\left(r_2\xi\right),\ \Upsilon_{57}=r_2^{-n},\ \Upsilon_{58}=r_2^{n},\ \Upsilon_{63}=-\bar{c}_{44}^{(2)}J_{p,r}\left(\frac{r_2\omega}{\beta_2}\right),$$

$$\Upsilon_{64}=-\bar{c}_{44}^{(2)}Y_{p,r}\left(\frac{r_2\omega}{\beta_2}\right),\ \Upsilon_{65}=c_{44}^{(3)}J_{p,r}\left(r_2\xi\right)+\frac{h_{15}^2}{\mu_3}J_{p,r}\left(r_2\xi\right),\ \Upsilon_{66}=c_{44}^{(3)}Y_{p,r}\left(r_2\xi\right)+\frac{h_{15}^2}{\mu_3}Y_{p,r}\left(r_2\xi\right),$$

$$\Upsilon_{67}=-nh_{15}r_2^{-n-1},\ \Upsilon_{68}=nh_{15}r_2^{n-1},\ \Upsilon_{73}=\gamma^{(2,3)}J_p\left(\frac{r_2\omega}{\beta_1}\right),\ \ \Upsilon_{74}=\gamma^{(2,3)}Y_p\left(\frac{r_2\omega}{\beta_1}\right),$$

$$\Upsilon_{75}=c_{44}^{(3)}J_{p,r}\left(r_2\xi\right)+\frac{h_{15}^2}{\mu_3}J_{p,r}\left(r_2\xi\right)-\gamma^{(2,3)}J_p\left(r_2\xi\right),$$

$$\Upsilon_{76}=c_{44}^{(3)}Y_{p,r}\left(r_2\xi\right)+\frac{h_{15}^2}{\mu_3}Y_{p,r}\left(r_2\xi\right)-\gamma^{(2,3)}Y_p\left(r_2\xi\right),\ \Upsilon_{77}=-nh_{15}r_2^{-n-1},\ \Upsilon_{78}=nh_{15}r_2^{n-1}\ ,$$

$$\Upsilon_{81}=\frac{h_{15}}{\mu_3}J_p\left(r_3\xi\right),\ \Upsilon_{82}=\frac{h_{15}}{\mu_3}J_p\left(r_3\xi\right),\ \Upsilon_{87}=r_3^{-n},\ \Upsilon_{88}=r_3^{n},\ Q_{11}=\sigma_{ext},\ X_{11}=C_1,\ X_{21}=C_2,$$

$$X_{31}=C_1^{(2)},\ X_{41}=C_2^{(2)},\ X_{51}=C_1^{(3)},\ X_{61}=C_2^{(3)},\ X_{71}=C_1^{*},\ X_{81}=C_2^{*}$$

ARTICLE IN PRESS

ARTICLE IN PRESS

References

[1] J. Franklin Mansur Rodrigues Filho, N. Tremblay, G. Soares da Fonseca, and P. Belanger, "The feasibility of structural health monitoring using the fundamental shear horizontal guided wave in a thin aluminum plate," *Materials*, vol. 10, no. 5, p. 551, 2017.

[2] H. Miao and F. Li, "Shear horizontal wave transducers for structural health monitoring and nondestructive testing: A review," *Ultrasonics*, vol. 114, p. 106355, 2021.

[3] C. Borigo, J. L. Rose, and R. K. Miller, "An Improved Shear-Horizontal Wave AE Sensor and an Explanation of SH Wave Mechanics," in *European Workshop on Structural Health Monitoring*, Springer, 2022, pp. 646–654.

[4] W. M. Ewing, W. S. Jardetzky, and F. Press, "Elastic waves in layered media," *Geologiska Föreningen i Stockholm Förhandlingar*, vol. 80, no. 1, pp. 128–129, 1958.

[5] J. Miklowitz, *The theory of elastic waves and waveguides*, vol. 22. Elsevier, 2012.

[6] S. Gupta, R. Dutta, and S. Das, "Flexoelectric Effect on SH-Wave Propagation in Functionally Graded Fractured Porous Sedimentary Rocks with Interfacial Irregularity," *Journal of Vibration Engineering & Technologies*, vol. 12, no. 1, pp. 1067–1087, Jan. 2024, doi: 10.1007/s42417-023-00894-9.

[7] R. Dutta, S. Das, H. Ahmad, M. A.R., and V. Gupta, "Comparative analysis of double and single porosity effects on SH-wave induced vibrations in periodic porous lattices," *Soil Dynamics and Earthquake Engineering*, vol. 186, p. 108919, Nov. 2024, doi: 10.1016/j.soildyn.2024.108919.

[8] M. A. R., R. Dutta, V. Gupta, A. Singhal, E.-M. Craciun, and S. Das, "Size-dependent analysis of surface wave in irregular fractured porous seabed subjected to fractional-order derivative," *Mechanics of Advanced Materials and Structures*, pp. 1–22, Jan. 2025, doi: 10.1080/15376494.2024.2440131.

[9] Q. Yang *et al.*, "Analysis of vortex-induced vibration in flexible risers using a physically-meaningful wake-oscillator model," *Eng. Struct.*, vol. 325, p. 119415, Feb. 2025, doi: 10.1016/j.engstruct.2024.119415.

[10] S. Wang, J. He, J. Fan, P. Sun, and D. Wang, "A time-domain method for free vibration responses of an equivalent viscous damped system based on a complex damping model," *Journal of Low Frequency Noise, Vibration and Active Control*, vol. 42, no. 3, pp. 1531–1540, Sep. 2023, doi: 10.1177/14613484231157514.

ARTICLE IN PRESS

[11] Z. Wang *et al.*, "Wave propagation in finite discrete chains unravelled by virtual measurement of dispersion properties," *IET Science, Measurement & Technology*, vol. 18, no. 6, pp. 280–288, Aug. 2024, doi: 10.1049/smt2.12193.

[12] S. K. Datta, "Ultrasonic and electromagnetic NDE for structure and material characterization engineering and biomedical applications," 2013, *Acoustical Society of America*.

[13] G. Hübschen, I. Altpeter, R. Tschuncky, and H.-G. Herrmann, *Materials characterization using nondestructive evaluation (NDE) methods*. Woodhead publishing, 2016.

[14] Y. Cao *et al.*, "Multi-Functional Self-Sensing Electronic Gasket for Structural Health Monitoring of Transportation Pipelines," *Adv. Funct. Mater.*, vol. 35, no. 20, May 2025, doi: 10.1002/adfm.202412634.

[15] J. Luo, Z. Cheng, N. Yu, Y. Tian, and J. Meng, "A flexible skin material with switchable wettability for trans-medium vehicles," *Int. J. Smart Nano Mater.*, vol. 16, no. 2, pp. 419–442, Apr. 2025, doi: 10.1080/19475411.2025.2504442.

[16] D. Zou, G. Liu, Z. Rao, T. Tan, W. Zhang, and W.-H. Liao, "A device capable of customizing nonlinear forces for vibration energy harvesting, vibration isolation, and nonlinear energy sink," *Mech. Syst. Signal Process.*, vol. 147, p. 107101, Jan. 2021, doi: 10.1016/j.ymssp.2020.107101.

[17] Y. He *et al.*, "Feasibility Study of Mechanical Stress Wave Detection in Power Semiconductor Devices Using Bare FBG Sensors," *IEEE Sens. J.*, vol. 25, no. 21, pp. 39849–39857, Nov. 2025, doi: 10.1109/JSEN.2025.3615108.

[18] J. L. Rose, *Ultrasonic guided waves in solid media*. Cambridge university press, 2014.

[19] Z. H. Tong, S. H. Lo, C. P. Jiang, and Y. K. Cheung, "An exact solution for the three-phase thermo-electro-magneto-elastic cylinder model and its application to piezoelectric-magnetic fiber composites," *Int. J. Solids Struct.*, vol. 45, no. 20, pp. 5205–5219, 2008, doi: 10.1016/j.ijsolstr.2008.04.003.

[20] Y. Li, X. Weng, D. Hu, Z. Tan, and J. Liu, "Data-Driven Method for Predicting Long-Term Underground Pipeline Settlement Induced by Rectangular Pipe Jacking Tunnel Construction," *J. Pipeline Syst. Eng. Pract.*, vol. 16, no. 3, Aug. 2025, doi: 10.1061/JPSEA2.PSENG-1855.

[21] X. Zhang, X. Liu, J. Jin, H. Wang, Z. Lv, and Y. Xiao, "Investigation of damage characteristics in freeze-thawed grey-white sandstone using AE multifractal analysis,"

ARTICLE IN PRESS

Geomechanics and Geophysics for Geo-Energy and Geo-Resources, vol. 11, no. 1, p. 93, Dec. 2025, doi: 10.1007/s40948-025-01023-4.

[22] C. Jia, S. Cheng, L. Li, and Y. Chen, "Seismic ahead-prospecting method based on delayed blasting excitation in the tunnel face: A case study," *Tunnelling and Underground Space Technology*, vol. 161, p. 106577, Jul. 2025, doi: 10.1016/j.tust.2025.106577.

[23] Z. Wang and X. Wang, "Quantum-Classical Hybrid Genetic Evolutionary Algorithm for Topology Optimization of Continuum Structures," *Int. J. Numer. Methods Eng.*, vol. 126, no. 13, Jul. 2025, doi: 10.1002/nme.70073.

[24] J. Gai, X. Yang, and Y. Zhao, "Electroacoustic wave scattering from cylindrical inhomogeneities in transversely isotropic piezoelectric composites," *Mater. Des.*, p. 115296, 2025.

[25] Q. Liu *et al.*, "Identifying vibration characteristics of hemispherical resonators with mass defects," *Int. J. Mech. Sci.*, p. 110856, 2025.

[26] X. Qiang, C. Wang, and H. Zhang, "Interval theory-embedded data-driven identification framework for uncertain thermo-elastic parameters," *Appl. Math. Model.*, p. 116743, 2026.

[27] H. Xu, M. Liu, J. Hu, and Y. Wang, "Enhanced electromagnetic wave absorption through in-situ mineralization constructed robust Fe3O4/PDA/Ti3C2Tx MXene composites with brick-and-mortar microstructure," *Ceram. Int.*, 2026.

[28] M. Nasr Esfahani, M. Hashemian, and F. Aghadavoudi, "The vibration study of a sandwich conical shell with a saturated FGP core," *Sci. Rep.*, vol. 12, no. 1, p. 4950, 2022.

[29] S. Dastjerdi, A. Alibakhshi, B. Akgöz, and Ö. Civalek, "On a comprehensive analysis for mechanical problems of spherical structures," *Int. J. Eng. Sci.*, vol. 183, p. 103796, 2023.

[30] A. E. Khosravi, F. Shahabian, and A. Aftabi Sani, "Dynamic examination of closed cylindrical shells utilizing the differential transform method," *Sci. Rep.*, vol. 14, no. 1, p. 15290, 2024.

[31] S. Dastjerdi, M. Malikan, V. A. Eremeyev, B. Akgöz, and Ö. Civalek, "On the generalized model of shell structures with functional cross-sections," *Compos. Struct.*, vol. 272, p. 114192, 2021.

[32] S. Dastjerdi, Ö. Civalek, M. Malikan, and B. Akgöz, "On analysis of nanocomposite conical structures," *Int. J. Eng. Sci.*, vol. 191, p. 103918, 2023.

ARTICLE IN PRESS

ARTICLE IN PRESS

[33] J. F. Doyle and J. F. Doyle, *Wave propagation in structures*. Springer, 1989.

[34] S. Gopalakrishnan, *Wave propagation in materials and structures*. Crc Press, 2016.

[35] S. Gopalakrishnan, *Elastic wave propagation in structures and materials*. CRC Press, 2022.

[36] M. Kliem *et al.*, "Damping analysis of cylindrical composite structures with enhanced viscoelastic properties," *Applied Composite Materials*, vol. 26, pp. 85–113, 2019.

[37] S. Panda, A. Gupta, and R. S. Reddy, "Viscoelastic composites for passive damping of structural vibration," in *Advanced Computational Methods in Mechanical and Materials Engineering*, CRC Press, 2021, pp. 221–250.

[38] S. D. Akbarov and T. Kepceler, "On the torsional wave dispersion in a hollow sandwich circular cylinder made from viscoelastic materials," *Appl. Math. Model.*, vol. 39, no. 13, pp. 3569–3587, 2015, doi: 10.1016/j.apm.2014.11.061.

[39] X. Zhang, Z. Li, X. Wang, and J. Yu, "The fractional Kelvin-Voigt model for circumferential guided waves in a viscoelastic FGM hollow cylinder," *Appl. Math. Model.*, vol. 89, pp. 299–313, 2021, doi: 10.1016/j.apm.2020.06.077.

[40] M. J. Khoshgoftar, A. Ghorbanpour Arani, and M. Arefi, "Thermoelastic analysis of a thick walled cylinder made of functionally graded piezoelectric material," *Smart Mater. Struct.*, vol. 18, no. 11, 2009, doi: 10.1088/0964-1726/18/11/115007.

[41] M. I. A. Othman and I. A. Abbas, "Generalized thermoelasticity of thermal-shock problem in a non-homogeneous isotropic hollow cylinder with energy dissipation," *Int. J. Thermophys.*, vol. 33, no. 5, pp. 913–923, 2012, doi: 10.1007/s10765-012-1202-4.

[42] X. Guo, P. Wei, L. Li, and M. Lan, "Effects of functionally graded interlayers on dispersion relations of shear horizontal waves in layered piezoelectric/piezomagnetic cylinders," *Appl. Math. Model.*, vol. 55, pp. 569–582, 2018, doi: 10.1016/j.apm.2017.11.029.

[43] M. Mahanty, P. Kumar, A. K. Singh, and A. Chattopadhyay, "On the characteristics of shear acoustic waves propagating in an imperfectly bonded functionally graded piezoelectric layer over a piezoelectric cylinder," *J. Eng. Math.*, vol. 120, no. 1, pp. 67–88, 2020, doi: 10.1007/s10665-019-10032-8.

[44] V. Gupta and M. S. Barak, "Photo-thermo-piezo-elastic waves in semiconductor medium subject to distinct two temperature models with higher order memory dependencies," *Int. J. Numer. Methods Heat Fluid Flow*, vol. 34, no. 1, pp. 84–108, 2024.

ARTICLE IN PRESS

[45] V. Gupta, M. Barak, and S. Das, “Impact of memory-dependent heat transfer on Rayleigh waves propagation in nonlocal piezo-thermo-elastic medium with voids,” *Int. J. Numer. Methods Heat Fluid Flow*, vol. 34, no. 4, pp. 1902–1926, 2024.

[46] V. Gupta, B. Barak, and S. Das, “Impact of memory-dependent heat transfer on Rayleigh waves propagation in nonlocal piezo-thermo-elastic medium with voids,” *Int. J. Numer. Methods Heat Fluid Flow*, vol. 34, no. 4, pp. 1903–1927, Mar. 2024, doi: 10.1108/HFF-10-2023-0615.

[47] V. Gupta, M. S. Barak, and S. Das, “Vibrational analysis of size-dependent thermo-piezo-photo-electric semiconductor medium under memory-dependent Moore–Gibson–Thompson photo-thermoelasticity theory,” *Mechanics of Advanced Materials and Structures*, vol. 31, no. 28, pp. 10543–10559, 2024.

[48] A. K. Yadav, M. S. Barak, and V. Gupta, “Reflection at the free surface of the orthotropic piezo-hygro-thermo-elastic medium,” *Int. J. Numer. Methods Heat Fluid Flow*, vol. 33, no. 10, pp. 3535–3560, 2023.

[49] S. Kumawat and S. K. Vishwakarma, “Circumferential SH wave in piezo-reinforced composite structure with imperfect interface bonding,” *Appl. Math. Model.*, vol. 123, pp. 311–331, 2023, doi: 10.1016/j.apm.2023.06.034.

[50] V. Gupta, S. Kumawat, S. K. Vishwakarma, M. S. Barak, and S. Das, “Effects of layer imperfections and material gradation on circumferential shear horizontal waves in cylindrical piezoelectric composite structure,” *Compos. Struct.*, vol. 359, no. September 2024, p. 118997, 2025, doi: 10.1016/j.compstruct.2025.118997.

[51] D. Royer and E. Dieulesaint, *Elastic waves in solids I: Free and guided propagation*. Springer Science & Business Media, 1999.

[52] A. J. M. Spencer, *Deformations of fibre-reinforced materials*. 1972.

[53] T. Li and Y. Wang, “Propagation Characteristics of SH Wave in Orthotropic Layer/Piezoelectric Column Structure,” *J. Phys. Conf. Ser.*, vol. 2381, no. 1, pp. 1–7, 2022, doi: 10.1088/1742-6596/2381/1/012070.

[54] M. S. Son and Y. J. Kang, “The effect of initial stress on the propagation behavior of SH waves in piezoelectric coupled plates,” *Ultrasonics*, vol. 51, no. 4, pp. 489–495, 2011, doi: 10.1016/j.ultras.2010.11.016.

[55] J. Yang, *An introduction to the theory of piezoelectricity*. Springer, 2005.

[56] J. M. Lee, K. H. Lee, B. M. Kim, S. K. An, and D. C. Ko, “Prediction of bending stiffness for laminated CFRP and its application to manufacturing of roof

ARTICLE IN PRESS

reinforcement," *Advances in Mechanical Engineering*, vol. 2014, 2014, doi: 10.1155/2014/404176.

[57] S. Dastjerdi, B. Akgöz, and Ö. Civalek, "On the shell model for human eye in Glaucoma disease," *Int. J. Eng. Sci.*, vol. 158, p. 103414, 2021.

[58] A. A. Khakhlenkova, A. E. Burov, and A. V Lopatin, "Deformation analysis of cylindrical lattice body of spacecraft in zone of high-pressure tank attachment," in *IOP Conference Series: Materials Science and Engineering*, IOP Publishing, 2021, p. 012011.

[59] S. Dastjerdi, M. Malikan, V. A. Eremeyev, B. Akgöz, and Ö. Civalek, "Mechanical simulation of artificial gravity in torus-shaped and cylindrical spacecraft," *Acta Astronaut.*, vol. 179, pp. 330–344, 2021.

[60] S. Dastjerdi, M. Malikan, B. Akgöz, Ö. Civalek, T. Wiczenbach, and V. A. Eremeyev, "On the deformation and frequency analyses of SARS-CoV-2 at nanoscale," *Int. J. Eng. Sci.*, vol. 170, p. 103604, 2022.

ARTICLE IN PRESS